

# Exploring the Similarities between Potential Smoothing and Simulated Annealing

REECE K. HART,<sup>1</sup> ROHIT V. PAPPU,<sup>2</sup> JAY W. PONDER<sup>3</sup>

<sup>1</sup>IBM T. J. Watson Research Center, P.O. Box 704, Yorktown Heights, New York 10598

<sup>2</sup>Department of Biophysics and Biophysical Chemistry, Johns Hopkins University School of Medicine, Baltimore, Maryland 21205

<sup>3</sup>Department of Biochemistry and Molecular Biophysics, Washington University School of Medicine, St. Louis, Missouri 63110

Received 8 May 1999; accepted 7 January 2000

**ABSTRACT:** Simulated annealing and potential function smoothing are two widely used approaches for global energy optimization of molecular systems. Potential smoothing as implemented in the diffusion equation method has been applied to study partitioning of the potential energy surface (PES) for *N*-Acetyl-Ala-Ala-*N*-Methylamide (CDAP) and the clustering of conformations on deformed surfaces. A deformable version of the united-atom OPLS force field is described, and used to locate all local minima and conformational transition states on the CDAP surface. It is shown that the smoothing process clusters conformations in a manner consistent with the inherent structure of the undeformed PES. Smoothing deforms the original surface in three ways: structural shifting of individual minima, merging of adjacent minima, and energy crossings between unrelated minima. A master equation approach and explicit molecular dynamics trajectories are used to uncover similar features in the equilibrium probability distribution of CDAP minima as a function of temperature. Qualitative and quantitative correlations between the simulated annealing and potential smoothing approaches to enhanced conformational sampling are established. © 2000 John Wiley & Sons, Inc. *J Comput Chem* 21: 531–552, 2000

**Keywords:** molecular mechanics; potential energy smoothing; diffusion equation method; conformational search; clustering; simulated annealing

Correspondence to: J. W. Ponder; e-mail: ponder@dasher.wustl.edu

Contract/grant sponsor: National Institutes of Health; contract/grant number R01-GM58712

## Introduction

Molecular conformations are often compared via a potential energy function that defines a potential energy surface (PES) over conformational space. Two separate issues arise in such studies: the accuracy of the potential energy function, and the tractability of adequately sampling the PES.<sup>1</sup> The topography of a multidimensional PES can be characterized by two types of measures: spatial scales and energy scales.<sup>2–4</sup> For a bistable system, the relevant spatial scales are the geometrical distance between the pair of local minima and the distance from each minimum to the top of the connecting barrier. In a multidimensional system, the diverse spatial scales correspond to the set of distances between all pairs of minima and distances between minima and connected transition states. Transitions between spatially distant regions will require large-scale conformational rearrangements, whereas small-scale changes will move the system to spatially proximal states.<sup>5</sup> Energy scales arise because multiple minima are separated by barriers, and the energy levels of minima and barriers span the entire spectrum of energy values.<sup>6,7</sup> A structured energy landscape is one for which the spatial and energy scales are correlated. If the correlation is strong, then similar conformations will have similar energies, as is the case for energy landscapes that resemble a funnel.<sup>7–10</sup> In energy landscapes with weaker correlations between spatial and energy scales, the distribution of energy barriers plays a central role, i.e., the energies of minima in spatially “distant” and distinct conformational states may, in fact, be similar, but the energy barriers separating these states are pronounced and cannot be easily negotiated.<sup>11–13</sup> The distinct states may either be true equilibrium conformations or nonequilibrium states as in structured glasses.<sup>14</sup> A disordered landscape is one for which there is no correlation between the two scales. This will be true of landscapes with randomly distributed minima and energy barriers.<sup>8</sup>

Potential energy surfaces of proteins and peptides can be hierarchically arranged, either in terms of the underlying energy scales<sup>15–17</sup> or in terms of spatial scales.<sup>2,18</sup> Such arrangements can help provide an understanding of methods that sample conformational space in a hierarchical manner. Hierarchical sampling is common to methods such as simulated annealing,<sup>19</sup> which operates on energy scales, and potential smoothing, which works on the spatial scales of a PES.<sup>20,21</sup>

Simulated annealing<sup>19</sup> is a widely used method for molecular structure optimization and refinement. The algorithm is derived by analogy to thermal annealing in condensed matter systems. In the physical annealing process, temperature is increased until a solid melts, then slowly reduced until the ground state of the solid is achieved. In simulated annealing, a system whose conformational energy is to be optimized is coupled to a heat bath initially set to a very high temperature. The temperature is then gradually lowered according to a prescribed cooling schedule, and conformational space is sampled for each value of the temperature. Instantaneous decrease of temperature from some high value leads to quenched or high-energy metastable states.<sup>22</sup> A practical advantage of simulated annealing is that a cooling schedule can be coupled to either a Metropolis Monte Carlo (MC)<sup>23</sup> or molecular dynamics (MD)<sup>24</sup> protocol without significant modification.

Aarts and Korst<sup>25</sup> have discussed the use of equilibrium Boltzmann statistics for analyzing specific features of simulated annealing, including conditions for asymptotic convergence to the global minimum, requirements of a cooling schedule, and different sampling weights that ensue as a function of varying temperature. For example, in Metropolis Monte Carlo simulated annealing acceptance ratios for putative transitions pass through a very sharp transition between the high- and low-temperature regions.<sup>25,26</sup> For large values of temperature,  $T$ , the average energy value and width of the distribution of energies approach constant values. The high temperature regime is characterized by acceptance ratio values,  $\chi$ , which tend to unity, while at low temperature,  $\chi \rightarrow 0$ .<sup>25</sup> It can be shown that simulated annealing will converge to the global minimum, providing the equilibrium Boltzmann distribution is attained at each temperature.

Obtaining an equilibrium distribution at each temperature requires inordinately lengthy sampling that grows exponentially with the size of the system.<sup>25–28</sup> Different ensembles result in the high- and low-temperature regimes, characterized by a drastic change in the equilibrium occupation probabilities of low energy regions with respect to the rest of the PES. At high temperatures all states become equally accessible leading to rapid interconversion, i.e., transitions over higher energy barriers are just as likely as transitions over lower energy barriers. As the temperature is lowered, the protocol confronts a very sharp transition to a regime where the equilibrium ensemble is radically different from the high-temperature regime.<sup>29</sup> Crossing

the transition region leads to a great reduction in excursions between states. For simulated annealing to be effective, either the low-lying regions need to be significantly populated for values of  $T$  higher than some threshold temperature, or the extent of sampling through the transition region has to be significantly enhanced so the system can populate low-lying regions. The Boltzmann machinery precludes the former, and the latter leads to the need for logarithmically slow cooling.<sup>25, 26</sup> Straub has developed a method to quantify the length of a simulated annealing trajectory in terms of two energy-scale parameters.<sup>26</sup> The number of steps along the cooling schedule can be determined to a first approximation by considering the ratio of the highest energy barrier connecting the global minimum to the rest of the PES, and the difference in energy between the global minimum and the second lowest energy state.

Hypersurface deformation refers to methods where the potential function to be sampled is physically altered either by an analytical transformation<sup>20, 21, 30–33</sup> or otherwise.<sup>34, 35</sup> Potential smoothing results from spatial averaging via methods that transform the potential function using a “smoothing kernel.” The result is a deformed PES, on which topographical features with the same spatial scale as the adjustable parameters of the “smoothing kernel” are averaged. For correlated energy landscapes, unstable and high-energy minima tend to be subsumed by lower energy basins.

A multidimensional potential energy function  $E(\mathbf{r})$  is replaced by a smoothed version of the function. The extent of spatial averaging is set by a scaling parameter  $t$ . The averaged version of the function is constructed via an integral transform of the original  $d$ -dimensional potential function as is shown in eq. (1).

$$U(\mathbf{r}_0, t) = \int \rho_G(\mathbf{r}, \mathbf{r}_0, t) E(\mathbf{r}) d\mathbf{r}, \quad (1)$$

where

$$\rho_G(\mathbf{r}, \mathbf{r}_0, t) = \frac{1}{(4\pi Dt)^{d/2}} \exp\left(-\frac{(\mathbf{r} - \mathbf{r}_0)^2}{4Dt}\right)$$

Here,  $\mathbf{r}_0$  denotes the Cartesian coordinates of the system measured in Å,  $t$  is a dimensionless deformation parameter, and  $D$  is a scaling coefficient in Å<sup>2</sup>, usually set to 1, such that the product  $Dt$  sets the size scale for spatial averaging. This is the form of potential smoothing first introduced by Scheraga and coworkers.<sup>20</sup>

In recent work we described three major features typical of potential smoothing.<sup>36</sup> Depending on the magnitude of  $Dt$  in eq. (1) vis-à-vis the length scales

of relevant distances on the PES the transformed function can have: (a) fewer minima due to the merging of minimum energy regions; (b) rank inversions or crossings in the relative energies of a pair of minima, i.e., two minima  $A$  and  $B$  with energies  $E_A < E_B$  on the undeformed surface can have energies  $E_A > E_B$  on a deformed surface; (c) and shifted spatial locations of minimum energy regions due to averaging effects.

For energy landscapes with a correlation between spatial and energy scales we propose that all features of potential smoothing will have analogs in simulated annealing. This will be apparent in: (a) the many-to-few mapping of minima; (b) similarities in the hierarchical clustering of conformationally related minima; (c) inversions in the relative weights of minima measured as Boltzmann weights for energy scaling and as deformed function values for spatial scaling; (d) shifted spatial locations of minima as a function of increased temperature/energy scaling or increased deformation/spatial scaling.

We note that previous work has been done to anneal approximations to classical distribution functions that also lead to smooth energy surfaces of the type shown in eq. (1).<sup>20, 31, 33, 37</sup> These methods suggest an implicit relationship between the extent of PES deformation and simulated annealing temperature that couples the fluctuations in energy scales to the fluctuations in spatial scales. Here, we decouple the two control parameters, deformation and temperature, to reflect upon an approach where the deformation parameter is set adiabatically.<sup>20, 38</sup>

A detailed analysis of a PES requires an exhaustive enumeration of all local minima and energy barriers. Enumeration of minima and transition states using traditional search methods is possible for systems with up to 20 degrees of freedom.<sup>39</sup> Small systems for which the PES can be exhaustively searched serve as useful models for complicated multidimensional systems. The current study uses a deformable OPLS (DOPLS) potential function to analyze the conformational space of a capped di-alanine peptide, *N*-Acetyl-Ala-Ala-*N*-Methylamide (CDAP). We have enumerated all minima and transition states on the CDAP potential energy surface, and provide a detailed characterization of conformational changes as a consequence of potential smoothing. Knowledge of the complete surface enables us to quantitatively demonstrate the analogies between potential smoothing and simulated annealing.

The next section describes aspects of a smoothable molecular mechanics potential, methods used

to generate a fully characterized PES, and the potential smoothing protocol. The Results section analyzes the network of minima and transition states on the undeformed PES for CDAP and the clustering of conformers on smooth surfaces. This is followed by qualitative and quantitative comparisons of important features of potential smoothing and simulated annealing. We conclude with a discussion of the implications of the analogy between potential smoothing and simulated annealing and comment on the CDAP conformational network.

## Methods

All calculations and structural manipulations were performed in Cartesian coordinates *in vacuo* using the TINKER molecular modeling package.<sup>40</sup>

### DEFORMABLE OPLS (DOPLS) POTENTIAL FUNCTION AND PARAMETERIZATION

The DOPLS potential function is a version of the original OPLS-UA potential function for proteins and peptides,<sup>41</sup> which is modified to enable potential smoothing. DOPLS is dependent on the same Cartesian coordinates  $\{\mathbf{r}\}$  as OPLS, as well as a parameter,  $t$ , which controls the extent of deformation. Equation (2) shows the individual energy terms of the DOPLS potential.

$$E_{total}(\mathbf{r}, t) = \sum_{bonds} E_{bond} + \sum_{angles} E_{angle} + \sum_{chiral} E_{improper} + \sum_{dihedrals} E_{torsion} + \sum_{atom\ pairs} E_{charge} + \sum_{atom\ pairs} E_{vdW} \quad (2)$$

Harmonic bond and angle terms are implemented as in standard OPLS. Chirality and planarity are enforced using a CHARMM<sup>42</sup> style improper torsional energy term, as shown in eq. (3). Harmonic improper torsions are used to impose planarity at  $sp^2$  atoms and chirality of  $sp^3$   $\alpha$ -carbon atoms. Parameters for the harmonic improper restraint term were derived by fitting to the minima of a standard OPLS trigonometric improper torsional energy term. The values used for the parameters in eq. (3) are shown in Table I.

$$E_{improper} = \frac{1}{2} K_{\Theta} (\Theta - \Theta_0)^2 \quad (3)$$

Because it is easy to compute analytical solutions for the integral transform in eq. (1) when applied to Gaussian functions, we use a Gaussian approximation<sup>30</sup> to the OPLS 12-6 Lennard-Jones

**TABLE I.**  
**Harmonic Improper Torsion Parameters.**

Atom Types	$k$ (kJ/mol/deg <sup>2</sup> )	$\Theta$ (deg)
C—CH <sub>3</sub> —N—O	251.0	0.00
N—C—C <sub><math>\alpha</math></sub> —H	23.0	0.00
C <sub><math>\alpha</math></sub> —N—C—CH <sub>3</sub>	732.0	36.5

These values were determined empirically by fitting OPLS-style trigonometric improper torsion to a CHARMM-style harmonic improper torsion with emphasis on small displacements from the ideal value.

potential as shown in eq (4),

$$E_{vdw} = \sum_{i=1}^{n_{gauss}} a_i e^{-b_i r^2}, \quad (4)$$

with

$$a_i = a_i^{\circ} \varepsilon_0, \quad b_i = b_i^{\circ} \left( \frac{2^{1/6}}{r_0} \right)^2, \\ \varepsilon_0 = \sqrt{\varepsilon_a \varepsilon_b} \quad \text{and} \quad r_0 = \sqrt{r_a r_b}$$

where  $\varepsilon_x$  and  $r_x$  are the Lennard-Jones parameters for atom  $x$ .  $\langle a_i^{\circ}, b_i^{\circ} \rangle$  are reference parameters chosen to fit a canonical Lennard-Jones function with well depth  $\varepsilon = 4.184$  kJ/mol and radius  $\sigma = 1$  Å;  $n_{gauss}$  is the number of Gaussians used in the approximation. We set  $n_{gauss} = 2$ ,  $\langle a_1^{\circ}, b_1^{\circ} \rangle = \langle 60614.0$  kJ/mol,  $905148$  Å<sup>2</sup> and  $\langle a_2^{\circ}, b_2^{\circ} \rangle = \langle -23.2353$  kJ/mol,  $1.22536$  Å<sup>2</sup>), which generates a very good fit over a wide range of interatomic distances.<sup>36</sup> A small van der Waals envelope of radius  $\sigma = 1$  Å and well depth  $\varepsilon = 0.04184$  kJ/mol is added to polar hydrogen atoms to prevent fusion with hydrogen bond acceptor atoms during large-scale conformational changes in potential smoothing.

Bond lengths, bond angles, and improper torsions are not altered as a function of increased deformation  $t$ . For values of  $t > 0$ , the DOPLS potential function uses the deformable functional form for the torsion, electrostatic and van der Waals terms as shown in eqs. (5)–(7) below, which are obtained using the corresponding undeformed functional forms  $E(\mathbf{r})$  in the integrand of eq. (1).

The deformed DOPLS torsional energy is computed as shown in eq. (5),

$$E_{torsion}(\omega, t) = \frac{1}{2} \sum_j V_j (1 + \cos(\omega j + \phi)) e^{-j^2 D_{torsion} t} \quad (5)$$

where  $j$  is the periodicity,  $V_j$  is the half-amplitude,  $\phi$  is the phase offset, and  $\omega$  is the dihedral angle value. The electrostatic energy is computed as shown in eq. (6),<sup>33</sup>

$$E_{\text{charge}}(r_{ij}, t) = \frac{q_i q_j}{4\pi \epsilon_0 r_{ij}} \operatorname{erf}\left(\frac{r_{ij}}{2\sqrt{D_{\text{charge}}t}}\right) \quad (6)$$

where  $q_i$  and  $q_j$  are the partial charges for atoms  $i$  and  $j$  and  $r_{ij}$  is the distance between these atoms. The deformable Gaussian approximation to the OPLS van der Waals energy is computed as shown in eq. (7),

$$E_{\text{vdw}}(r_{ij}, t) = \sum_{i=1}^{n_{\text{gauss}}} \frac{a_i}{(1 + 4b_i D_{\text{vdw}} t)^{3/2}} \times \exp\left(\frac{-b_i r_{ij}^2}{(1 + 4b_i D_{\text{vdw}} t)}\right) \quad (7)$$

where  $a_i$  and  $b_i$  are as in eq. (4).

The parameter  $t$  controls the extent of potential surface smoothing.  $D_{\text{torsion}}$ ,  $D_{\text{charge}}$ , and  $D_{\text{vdw}}$  are tunable scaling coefficients that control the relative length scales over which individual terms are smoothed. In the current work, we use  $D_{\text{torsion}} = 0.0225$  (radian)<sup>2</sup>,  $D_{\text{charge}} = 1$  Å<sup>2</sup>, and  $D_{\text{vdw}} = 1$  Å<sup>2</sup>. These values were chosen based on an estimate of the range and analysis of the type of space, Cartesian vs. torsional, accessible to each term.<sup>36</sup>

The DOPLS potential for  $t = 0$  closely approximates the original OPLS potential function for all reasonable low energy conformations. The average deviation of the OPLS and  $t = 0$  DOPLS potentials is 0.07 kJ/mol at the 142 minima and 0.15 kJ/mol at the 1038 transition states discovered by grid search, as described below. Analytical first and second derivatives of all terms in DOPLS are used in energy minimizations.

## MINIMIZATION AND CONFORMATIONAL REDUNDANCY

All minimizations were performed using a preconditioned truncated Newton conjugate gradient method with finite difference matrix-vector product<sup>44</sup> to a gradient convergence criterion of  $10^{-4}$  kJ/mol/Å per atom. Two minimum energy conformations are considered to be identical if the root-mean-squared deviation (rmsd) from the superposition of all atoms is less than 0.001 Å. In determining which members in a set of  $N$ -conformations are identical, we obviated a full pairwise  $O(N^2)$  comparison by superposing only those pairs of structures within an energy window of 0.01 kJ/mol. The use of a strict convergence criterion during min-

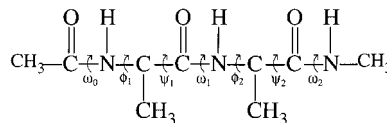


**FIGURE 1.** Capped Dialanine Peptide (*N*-Acetyl-Ala-Ala-*N*-Methylamide, CDAP). Methyl groups are represented as united atoms. The system has 18 atom centers, 48 dimensional Cartesian conformational space, and 7 rotatable bonds.

imization facilitates the use of energies to discriminate distinct structures. All conformational pairs determined to be identical by superposition had energies equal to seven significant digits.

## GENERATION OF CAPPED DIALANINE PEPTIDE (CDAP) CONFORMATIONS

The skeletal structure of *N*-Acetyl-Ala-Ala-*N*-Methylamide (CDAP) is shown in Figure 1. CDAP conformations were generated from all combinations of *cis* or *trans* peptide bonds and the nine  $\langle\phi, \psi\rangle$  pairs corresponding to canonical low energy regions listed in Figure 2.<sup>45</sup> This enumeration resulted in a set of  $2 \times 9 \times 2 \times 9 \times 2 = 648$  conformations. After minimization from each starting conformation, 136 unique minima remained. Each minimum

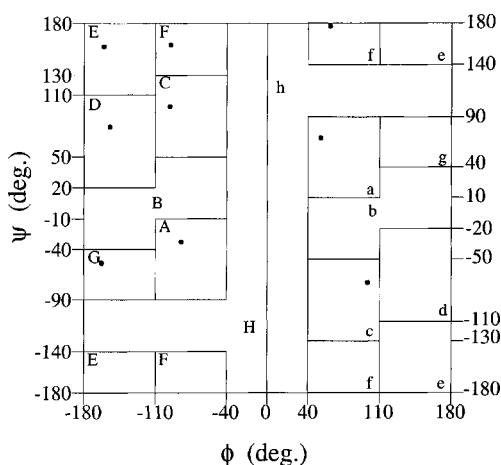


**FIGURE 2.** Sixteen conformational regions of a Ramachandran map identified by Zimmerman et al.<sup>38</sup> The nine  $\langle\phi, \psi\rangle$  regions used for grid search are denoted by filled circles. The  $\langle\phi, \psi\rangle$  torsion angle descriptors of the conformational code were specified as follows (conformer region:  $\phi, \psi$ ): (A:  $-75^\circ, -45^\circ$ ), (C:  $-85^\circ, 80^\circ$ ), (D:  $-150^\circ, 70^\circ$ ), (E:  $-155^\circ, 155^\circ$ ), (F:  $-85^\circ, 155^\circ$ ), (G:  $-160^\circ, -60^\circ$ ), (a:  $55^\circ, 60^\circ$ ), (c:  $80^\circ, -65^\circ$ ), (f:  $65^\circ, 180^\circ$ ).  $\omega$  values of  $0^\circ$  are *cis* and  $180^\circ$  are *trans*.

was assigned an identifier equal to its energy rank (global minimum is structure 1, etc.) and a conformational code. The conformational code consists of five descriptors, one for each of the three peptide bonds and the two  $\langle\phi, \psi\rangle$  pairs in CDAP. Peptide bonds were classified as *cis* (c) or *trans* (t). A  $\langle\phi, \psi\rangle$  descriptor is a letter corresponding to one of the 16 regions shown in Figure 2. As described in the Results section, subsequent analysis added six additional minima to the initial set of 136, resulting in a total of 142 minima.

## PATHS AND TRANSITION STATES

To fully characterize the PES, all transition states were located. Conformational paths connecting pairs of minima were calculated using the reaction path method of Czerminski and Elber.<sup>13, 46</sup> The local energetic maxima along each path were minimized to the nearest stationary point via a truncated Newton method. Transition states were identified as the subset of unique stationary points whose Hessians had exactly one negative eigenvalue. Because the Czerminski and Elber method is biased by a path directionality, paths in both directions were investigated.

Each transition state connects a pair of minima on the potential surface. In some cases, more than one transition state connects the same pair of minima. The minima directly connected by a transition state were identified using the following scheme: (1) two conformations were generated by perturbing away from the transition state by a small displacement in each direction along the mode corresponding to the negative eigenvalue, (2) the structures were minimized, (3) the identity of each minimized conformation was determined by comparison with known minima using the redundancy criterion described above.

## POTENTIAL SMOOTHING PROTOCOL

The potential smoothing protocol consists of a series of minimizations on increasingly deformed potential surfaces corresponding to increasing values of the deformation parameter  $t$ . We refer to the PES smoothed using  $t = t_i$  as the  $t_i$  surface. The undeformed potential surface is defined by  $t = t_0 = 0$ . In the first stage of the protocol ( $i = 1$ ), each minimum on the  $t_0$  surface is minimized on the smoother  $t_1 = t_0 + \Delta t$  surface. For iteration  $i$  of the protocol, each conformation on the  $t_{i-1}$  surface is minimized on the  $t_i$  surface. As surfaces become smooth, minima that are distinct on the  $t_{i-1}$  surface may merge

into a single minimum on the smoother  $t_i$  surface. At the end of every iteration, we record the identities of minima that merge and the number of unique minima that remain. The rate of deformation is dictated by a schedule of  $n$  steps in the range  $[0, t_{\max}]$  given by

$$t_i = t_{\max} \left( \frac{i}{n} \right)^q, \quad 1 \leq i \leq n$$

We used  $t_{\max} = 60$ ,  $n = 120$ , and  $q = 2$ . A single minimum remains on the CDAP surface for all  $t \geq 51.27$ . The chosen smoothing schedule results in a gradual clustering of conformations and provides sufficient detail to analyze small changes in the PES. Similar results are obtained for slower ( $n = 2000$ ) or faster ( $n = 20$ ) rates of smoothing and for linear ( $q = 1$ ), cubic ( $q = 3$ ), or quartic ( $q = 4$ ) schedules.

---

## Results

CDAP was chosen for this study because its small size allowed a thorough search for minima and transition states on the undeformed surface. This network of conformations enabled detailed analysis of changes to the PES features during potential smoothing, comparison of conformational clustering by potential energy barriers and potential smoothing, and comparison of specific features of potential smoothing and simulated annealing.

---

### Details of the CDAP Potential Energy Surface

Reaction paths were initially computed between all 4262 pairs of the 136 minima that differed by zero (2), one (864), or two (3396) conformational descriptors. This resulted in 667 unique transition states of which 75 represented paths connecting minima differing by three descriptors. Previous results for isobuturyl-(ala)<sub>3</sub>-NH-methyl (IAN) on the CHARMM PES<sup>13</sup> suggested that transition states between minima differing in three degrees of freedom seldom occur. Next, we computed the 7128 reaction paths between all pairs of minima that differed by three descriptors, and found 312 additional unique transition states. By this point, 10,806 of  $136 \times 135 = 18,360$  possible directed reaction paths had been computed, so all remaining reaction paths were computed leading to 59 additional transition states. No transition states connected minima that differed by more than three descriptors.

Minimization from  $667 + 312 + 59 = 1038$  unique transition states led to the discovery of six new high-lying minima. These were 130–170 kJ/mol above the global minimum, and connected to existing minima by energetic barriers less than 0.6 kJ/mol. The six new minima were added to the pool of unique minima and the remaining pairwise paths were computed; no new minima or transition states were found. Because all minimizations converged to known minima, we believe that the set of local minima and transition states found from the grid search represents an exhaustive enumeration of the topographical features of the PES. The resulting network consists of 142 unique minima and 1038 unique transition states that form a connected network of conformations. There exists at least one sequence of paths from every minimum to every other minimum on the potential energy surface.

The distributions of minima and transition state energies are shown in Figure 3. A summary of the 10 lowest energy conformations, which are all within 15 kJ/mol of the global minimum, is presented in Table II. Conformations for the four lowest minima are shown in Figure 4.

A number of important features of the PES topography were obtained by analysis of the transitions directly accessible to each minimum. For every transition state,  $ts$ , which connects minima  $m_1$  and  $m_2$ , with energies  $E_{ts}$ ,  $E_{m_1}$ , and  $E_{m_2}$ , respectively, such that  $E_{m_1} < E_{m_2}$ , we computed the high-to-low energy barrier ( $E_b = E_{ts12} - E_{m_2}$ ). When multiple transition states connect the same pair of minima, we used the transition state with the lowest energy. The smallest barriers are typically between high-lying minima. There does not appear to be any

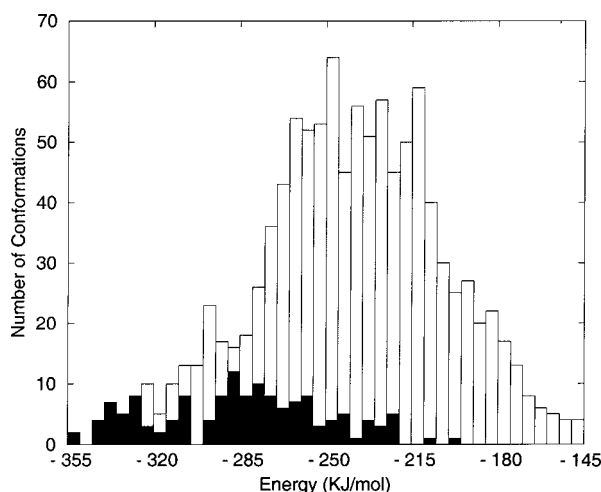


**FIGURE 3.** The distribution of energies of 142 unique minima (filled bars) and 1038 unique transition state conformations (unfilled bars) on the undeformed DOPLS PES. The bin size is 5 kJ/mol.

obvious correlation between  $E_b$  and the energies of the minima. There are, on average, 15 paths connecting a given minimum to the rest of the PES, and the number of paths connecting each minimum ranges between 1 and 67. Higher energy minima tend to be connected by fewer paths than those at lower energy, suggesting greater flux into the lower energy regions. The lowest energy structure is a deep well connected via 67 transition states. This apparent density of reaction paths belies the fact that all transitions from minimum 1 to other minima are via barriers of 44.7 kJ/mol or more. Other low-energy minima typically have several pathways over much smaller barriers. For instance, minimum 2 has five

**TABLE II.**  
**Ten Minima within 15 kJ/mol of the Global Minimum.**

Id	$E$ (kJ/mol)	$\omega_0$ (deg)	$\phi_1$ (deg)	$\psi_1$ (deg)	$\omega_1$ (deg)	$\phi_2$ (deg)	$\psi_2$ (deg)	$\omega_2$ (deg)	Conf. Code
1	-352.2535	+174	-99	+118	-5	-119	+100	-177	tCcDt
2	-351.1075	-178	-83	+67	-176	-82	+65	-179	tCtCt
3	-343.0721	-178	-84	+68	-178	+65	-54	+179	tCtct
4	-342.8826	+173	-153	+167	+174	-152	+166	-179	tEtEt
5	-342.8717	+174	-149	+162	-179	-84	+72	-178	tEtCt
6	-342.0407	+179	+64	-55	+178	-82	+67	-179	tctCt
7	-338.9203	-179	-77	+77	-174	-174	-39	+178	tCtBt
8	-337.9781	-179	+59	-74	+177	-101	-15	-179	tctAt
9	-337.9781	-169	-79	-6	+173	-124	+29	-179	tBtDt
10	-337.1430	+177	-88	+77	+176	-142	+157	-178	tCtEt

The columns are structural identifier (energetic rank on the undeformed DOPLS PES), energy, backbone dihedral angles (see also Fig. 1), and conformational code. Structures of minima 1–4 are depicted in Fig. 4.

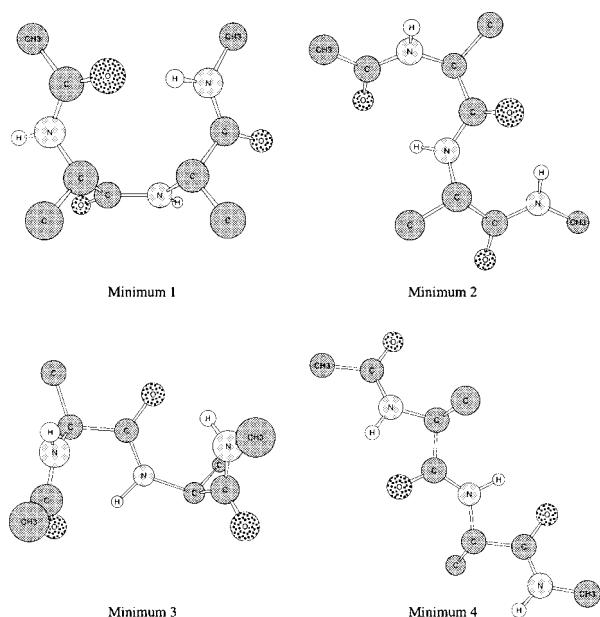


**FIGURE 4.** The four lowest energy structures for CDAP. See also the listing in Table II.

reaction paths over barriers below 20 kJ/mol, and nine below 44.7 kJ/mol.

Paths between minima were classified by the number of conformational descriptors that differ between the incident minima. We observed paths between minima that differed by zero, one, two, and three descriptors. Of 17 paths that connect minima differing by zero descriptors, 14 are self-connecting or “degenerate rearrangement” paths.<sup>47</sup> We note that a large number of paths connected minima that differed by three descriptors. We investigated the structural differences between these conformers more carefully by computing the Euclidean distance spanned by a path for both  $\langle\phi_1, \psi_1\rangle$  and

$\langle\phi_2, \psi_2\rangle$  as shown in eq. (8):

$$d_i = \sqrt{(\Delta\phi_i)^2 + (\Delta\psi_i)^2}, \quad (8)$$

where

$$\Delta\omega_i = \min(|\omega_{i,a} - \omega_{i,b}|, 360 - |\omega_{i,a} - \omega_{i,b}|)$$

for  $\omega \in \{\phi, \psi\}$ . Here,  $d_i$  is the  $\langle\phi_i, \psi_i\rangle$  Euclidean distance between structures  $a$  and  $b$ . This was done to ensure that the conformational descriptors do not overestimate the significance of conformational changes. The results are summarized in Table III, and clearly show that a significant number of paths spanned large distances of conformational space.

In the following sections we compare specific features of simulated annealing and potential smoothing using the fully enumerated PES of CDAP. These features include partitioning of the PES into macrostates or basins, the efficiency of each method in converging to the global minimum, shifting of minima due to spatial or ensemble averaging, and crossings between pairs of minima.

### Partitioning the CDAP PES Based on Energetic Barriers and Potential Smoothing

We use the term “clustering” to refer to the partitioning of a set of conformations into mutually exclusive subsets. An agglomerative clustering algorithm equivalent to that used by Shenkin and McDonald<sup>47</sup> was employed. For a system with  $N$  conformations, there are  $N(N-1)/2$  possible generalized pairwise distances. Agglomerative clustering identifies the  $N-1$  shortest edges that join conformations in a connected network. We associate a directionality with each edge based upon the energies of the connected conformations, for example,

**TABLE III.** Summary of Paths in the CDAP Network.

Redundancy	Number of Changed Descriptors				
	Loopback	0	1	2	3
Unique	7	2	306	243	130
Total	14	3	489	345	187
$\langle d_1 \rangle \pm \text{SD} (^\circ)$		$16 \pm 10$	$66 \pm 77$	$86 \pm 69$	$113 \pm 58$
$\langle d_2 \rangle \pm \text{SD} (^\circ)$		$111 \pm 74$	$72 \pm 76$	$98 \pm 67$	$111 \pm 60$
$\langle E_b \rangle \pm \text{SD} (\text{kJ/mol})$	$77 \pm 58$	$6 \pm 7$	$32 \pm 26$	$44 \pm 27$	$64 \pm 23$

There are 1038 paths between 688 unique pairs of minima. The table shows the average Euclidean distance between minima in  $\langle\phi, \psi\rangle$  space [see eq. (8)] and the average minimum energy barrier.



minimum  $m_1$  merges into  $m_2$ . The result is a set of  $N - 1$  ordering relations that are represented by tree diagrams in which branches of a tree represent families of structures or conformational basins. Trees depict two important pieces of information: (1) the greatest separation of structures within a single basin, and (2) the minimum separation between structures in different basins. For example, a branch point that joins branches  $b_1$  and  $b_2$  at five units indicates: (1) that every conformer in basin  $b_1$  is separated from every other conformer in  $b_1$  by no more than five units, and (2) that every conformer in basin  $b_1$  is separated from every conformer in  $b_2$  by at least five units.

In this work, structures were clustered in two distinct ways, based upon the extent of deformation  $t$  and upon the energy barrier  $E_b$ . For clustering on deformed surfaces, the distance between structures is the deformation  $t$ , at which they merge. In energetic clustering, the clustering distance is the lowest high-to-low energy barrier,  $E_b$ .

### CLUSTERS DERIVED BASED ON ENERGY SCALES

The energy barrier from the minimum of higher energy to that of lower energy was used as one measure of the distance between a pair of minima. Specifically, for each path between minima  $A$  and  $B$  connected by transition state  $AB$  with energies  $E_A$ ,  $E_B$ , and  $E_{AB}$ , respectively, we associate the minimum energy barrier  $E_b = \min(E_{AB} - E_A, E_{AB} - E_B)$ . In cases where minima  $A$  and  $B$  are connected by multiple paths, we used the minimum  $E_b$  value for the connection. A similar scheme has been used by Becker and Karplus<sup>10</sup> to generate a canonical disconnectivity graph for IAN to partition the PES into temperature-dependent basins. The energy barrier  $E_b$  can be associated with a thermal energy barrier  $K_B T$ , and  $K_B$  is Boltzmann's constant. We associate with each transition the energy barrier traversed in crossing from the higher to lower energy minimum by analogy to simulated annealing wherein a system becomes gradually confined to low-energy regions because the transitions out of these regions become less probable with decreasing temperature. Thus, barriers act as a one-way trap whose effect is to localize a system in regions of low energy. A minimum subsumes all higher energy minima that are connected to it via barriers less than or equal to some threshold energy,  $E^*$ . We use the identifier of the structure of lowest energy conformation within a basin as a representative of the basin and conformations therein. The result of this clustering is

shown in Figure 5.  $E^*$  is equivalent to a threshold thermal barrier  $K_B T$  where  $T$  may be the temperature of a heat bath coupled to the system.

### CLUSTERS DERIVED FROM SPATIAL SCALING

Topographical changes that occur during potential smoothing are characterized by three processes: shifting in the location of minima, energy rank inversion, and merging. These effects and their influence on the smoothing protocol are depicted in Figure 6 and discussed below.

We refer to the translation of basins in conformational space during potential smoothing as shifting. The displacement of  $\langle \phi_1, \psi_1 \rangle$  and  $\langle \phi_2, \psi_2 \rangle$  on Ramachandran maps depends on the proximity, relative depth of minima, and the number of minima that constitute the basin. In Figure 6, minimum  $C_0$  on the  $t = 0$  surface is minimized on the  $t = t_1$  surface. This causes the conformation to shift to a slightly changed conformation,  $C_1$ .

The rank energy order of a pair of minima may invert, which we refer to as a crossing. Crossing is depicted in Figure 6 by minima  $A_1$ ,  $B_1$ ,  $A_2$ , and  $B_2$ . Notice that  $E(A_1) < E(B_1)$  on the  $t = t_1$  surface but  $E(A_2) > E(B_2)$  on the  $t = t_2$  surface, where  $t_2 > t_1$ . Crossings have serious consequences when potential smoothing is applied to global optimization, and techniques have been developed to circumvent this effect.<sup>25,41</sup>

Two unique minima  $m_i$  and  $m_j$  can undergo a merging into a common basin at some deformation value  $t_m$ . If the two minima are equal in depth and width on the undeformed surface, then a merging of these two minima will result from eliminating the barrier and an equal translation of the two minima into the new basin. If the original energy gap between the minima is pronounced, then the higher lying minimum slides into the broader basin of the lower lying minimum, i.e., the position of the new single minimum is close to the location of the lower minimum from the undeformed surface. To be faithful to the crossing phenomenon identified above, we chose the convention of using the energies at the previously deformed surface rather than the undeformed PES to determine a merge direction. Thus, minimum 4 is the root of the tree in Figure 8 because it crossed with minimum 1 on the  $t = 1.22$  surface. If the deformation process is characterized by crossing-free mergings, then the minimum that survives on the highly deformed surface is related to the global minimum. Merging is depicted in Figure 6 using minima  $C_1$ ,  $D_1$ , and  $C_2$ . When conformations  $C_1$  and  $D_1$  on the  $t = t_1$  surface are

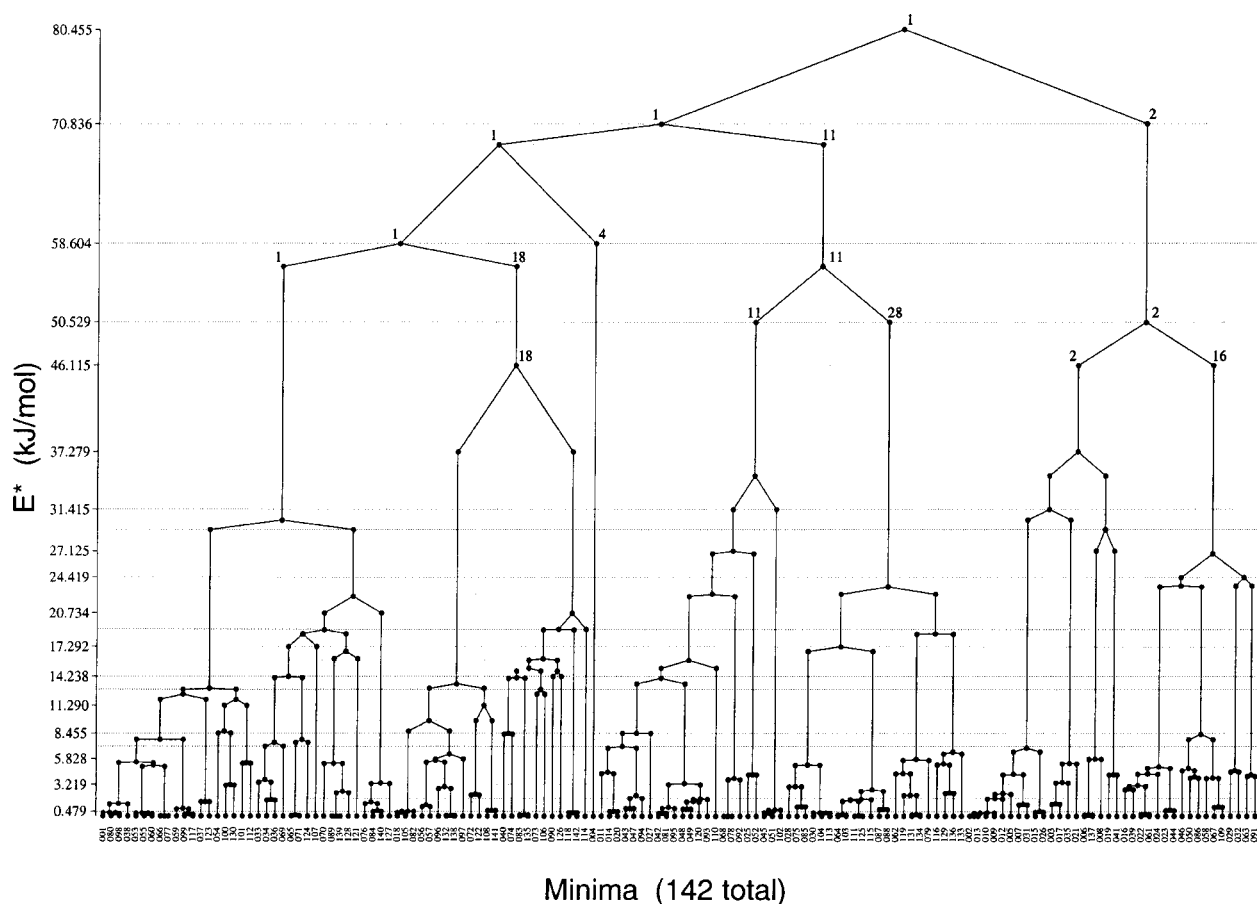


**FIGURE 5.** Energy barrier clustering of minima. All minima within a branch are connected by barriers not greater than the value on the ordinate. The two most energetically distinct basins are 1 and 2. There is no pair of minima, one from basin 1 and one from basin 2, connected by a barrier less than 80.455 kJ/mol. The eight structures at  $E^* = 38$  kJ/mol are used for comparison with potential smoothing.

minimized on the  $t = t_2$  surface, they converge to the same conformation  $C_2$ .

In the case of CDAP, distant regions of conformational space are typically clustered as a single merging of one basin into another. The  $\langle\phi, \psi\rangle$  centers of basins are essentially stationary until they merge. In other words, basins merge not because their representative centers are gradually drawn together, but because the barrier between them is eliminated. The surviving minimum that represents a basin of conformations is usually located near the lower of the two merging minima. This observation is important because it suggests that a basin of structures is located near a conformation that represents the most prevalent members of the basin, not a meaningless average structure.

Evolution of minima on the  $t = 0, 0.61, 1.08, 1.69$  surfaces is shown in Figure 7. The 142 minima on the undeformed  $t = 0$  PES are scattered over all quadrants of the  $\langle\phi, \psi\rangle$  map and aggregate into several

groups within each quadrant, nominally occupying the canonical  $\alpha_R$ ,  $\alpha_L$ , and  $\beta$  regions, and a low-energy region near  $(+50, -50)$ . At  $t = 0.610$ , the degree of dispersion is reduced but all quadrants are still occupied. For  $t = 1.08$ , all of the 142 local minima from the undeformed surface merge into basins centered around the  $\alpha_R$  and  $\beta$  regions. This clustering result holds true for both pairs of soft torsional modes,  $\langle\phi_1, \psi_1\rangle$  and  $\langle\phi_2, \psi_2\rangle$ .

Figure 7 illustrates several important trends in the clustering of minima on smooth surfaces. Sixty-three percent of the 142 local minima for CDAP have  $\langle\phi_1, \psi_1\rangle$  and  $\langle\phi_2, \psi_2\rangle$  values between the A, G, C, D, E, or F regions of  $\phi$ - $\psi$  space. These regions represent the canonical  $\beta$ -strand or  $\alpha_R$  regions. Furthermore, the lower energy conformers including the global minimum have  $\langle\phi_1, \psi_1\rangle$  and  $\langle\phi_2, \psi_2\rangle$  angle values in these regions. Minima with  $\langle\phi_1, \psi_1\rangle$  and  $\langle\phi_2, \psi_2\rangle$  values from the right half of the  $\phi$ - $\psi$  plane merge into basins from the left half of the  $\phi$ - $\psi$  plane, as shown

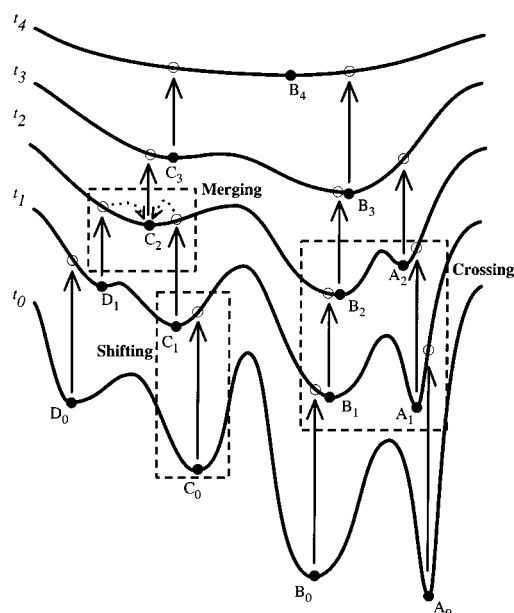


**FIGURE 6.** Illustration of topographical changes during potential smoothing. The original PES ( $t_0$ ) appears at the bottom. PESs at increasing deformations are offset vertically for clarity. Potential smoothing is characterized by three processes: shifting, merging, and crossing. Solid arrows depict an adiabatic change of deformation for a given conformation. Dotted black arrows denote minimizations. Minima are indicated by filled circles.

in Figure 7. Because basins do not migrate significantly except when merging, conformational search on deformed surfaces provides a meaningful sampling of the conformations represented by a basin.

For every level of the smoothing protocol, the merging of minima is recorded. We interpret the value of  $t$  at which such a merging occurs as a “distance” between the conformations that merge. Because redundant structures are eliminated throughout the smoothing protocol, we obtain exactly 141 mergings. From these “distances,” a tree of the potential smoothing clustering process is generated as shown in Figure 8.

### COMPARISON OF ENERGY SCALE AND SPATIAL SCALE CLUSTERS

We compare the two clusters when both measures reduce the original set of 142 minima to eight basins. This corresponds to a deformation level of  $t = 1.69$  (Fig. 8) and an energy barrier of  $E^* = 38$  kJ/mol (Fig. 5). In Figures 5 and 8, minima that constitute a basin are leaves of the tree that appear beneath a branch.

The clustering techniques are compared by examining which minima are clustered together and the structural similarities and differences in each basin.

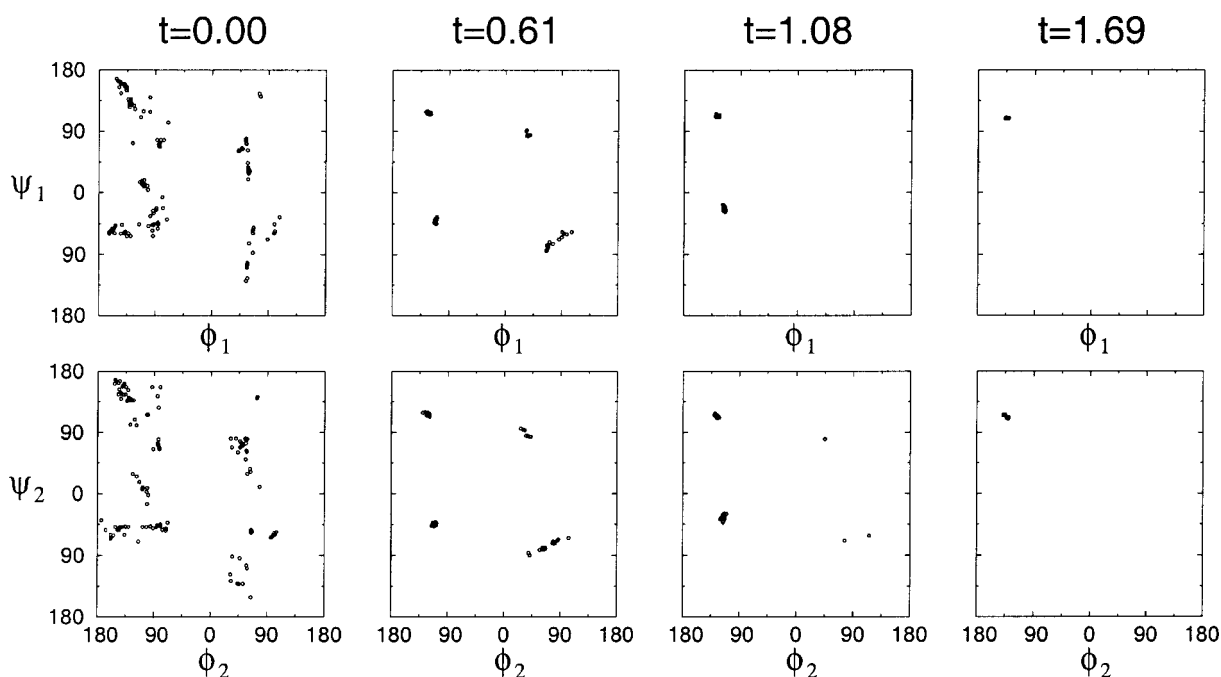


**FIGURE 7.** Ramachandran plots of  $(\phi_1, \psi_1)$  (top) and  $(\phi_2, \psi_2)$  (bottom) for four levels of surface deformation:  $t = 0, 0.61, 1.08, 1.69$ . The deformations shown were chosen to exemplify features of the clustering or differences between the two sets of dihedrals and are typical for other deformations.

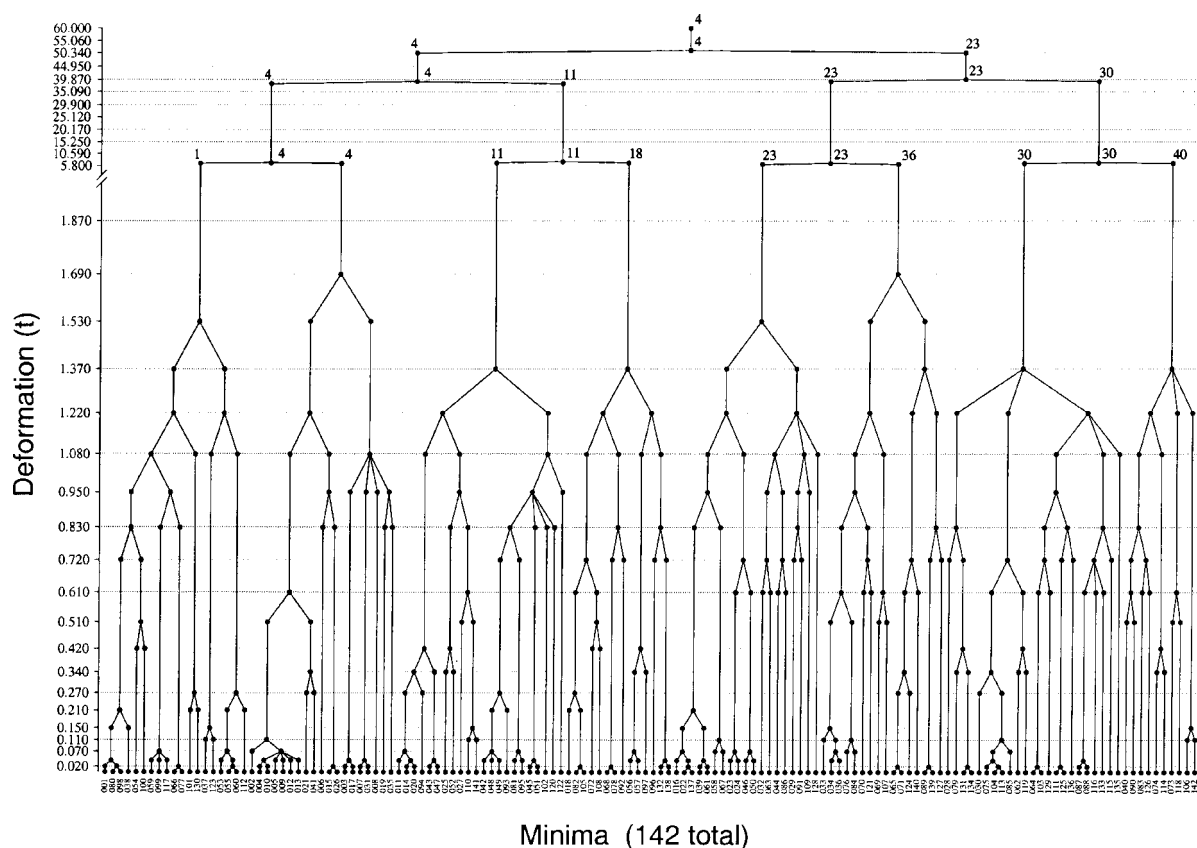


**FIGURE 8.** Clustering of minima as the CDAP PES is smoothed. The 142 minima enumerated by grid search appear as leaves of the tree at the bottom of the figure. The ordinate is the extent of deformation and is discontinuous for sake of readability. As deformation increases (from bottom to top), minima merge into basins. The eight structures at  $t = 1.69$  are the basis for much of the analysis in the text.

Similarities between the two types of clustering for  $t = 1.69$  and  $E^* = 38$  kJ/mol are shown in Table IV. If the two methods are exactly equivalent, the overlap of members for each basin would be identical, and Table IV would contain no off-diagonal elements. This is true for all but the intersection of the E1 and S36 basins. E1 consists of a total of 36 conformers of which 19 are *trans-cis-trans* ( $\omega_0$ - $\omega_1$ - $\omega_2$ ) and 17 are *cis-cis-trans* conformers. The total population of S1 is 19 *trans-cis-trans* conformers. The overlap of E1 and S1 are the 19 *trans-cis-trans* conformers. The remaining 17 *cis-cis-trans* conformers in E1 are split between S36 and S23. This establishes that clustering in terms of potential smoothing shows more uniformity in conformational types compared to clustering in terms of energy barriers. Both methods reduce the PES into a smaller set of basins leading to a hierarchical description of the PES. For CDAP, the ordering of the energy barriers is in keeping with the length scales of the PES.

We establish the connectivity of the minima on the  $t = 1.69$  surface as was done for all minima

on the undeformed DOPLS surface. At this level of smoothing, the system exhibits all eight permutations of the three *cis* or *trans* peptide bond conformations. A diagram of this network is shown in Figure 9. Further collapse of this cube occurs by nearly simultaneous merging of parallel transitions:  $\omega_1$  (minimum  $1 \rightarrow 4$ ,  $36 \rightarrow 23$ ,  $18 \rightarrow 11$ ,  $40 \rightarrow 30$ ) for  $t \approx 7$ ,  $\omega_2$  ( $11 \rightarrow 4$ ,  $30 \rightarrow 23$ ) for  $t \approx 39$ , and  $\omega_0$  ( $23 \rightarrow 4$ ) for the  $t = 51.27$  surface. It is important to emphasize the structural significance of the clustering represented in Figure 9. The barrier to rotation of a single peptide bond is  $\sim 84$  kJ/mol, and is expected to be the origin of the most prominent features of the undeformed surface. Each of the eight minima remaining on the  $t = 1.69$  surface represent a combination of these three structural characteristics. For large values of  $t$ , the smoothing process simplifies the original PES by clustering conformations into basins according to the largest PES features, i.e., *cis-trans* isomers.

**TABLE IV.**  
Comparison of Clustering by the Energy Barrier and Potential Smoothing Methods at Levels where Eight Basins Remain ( $t \leq 1.69$ ,  $E^* \leq 38$  kJ/mol).

PS	EB pop.	1	2	11	18	16	28	4	40
		36	19	23	13	17	22	1	11
1	19	19							
4	19		18					1	
11	22			20					
18	14				11				
23	19	1	1			17			
30	23						22		
36	16	16							1
40	10								10

Each basin represents a set of structures on the original PES clustered by either energy barrier or potential smoothing. The number of structures in the intersection of each potential smoothing basin with each energy barrier clustering basin suggests the extent to which the two techniques cluster similarly. We identified each basin by the member with the lowest energy. It is important to note that the basin names are irrelevant; only the identities of the conformers from the undeformed surface that cluster similarly by energetic barrier and potential smoothing are meaningful.

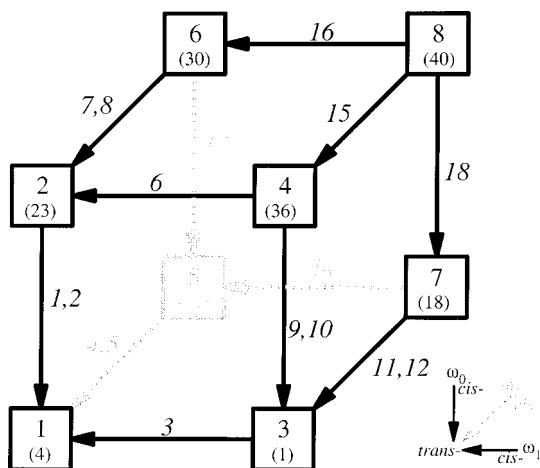


**FIGURE 9.** Network of conformations remaining at  $t = 1.69$ . The eight remaining structures represent all combinations of *cis-trans* interconversions of the three peptide bonds, and are denoted by the vertices of the cube. Each vertex shows the rank of the energy on this surface and the structure identifier in parentheses for comparison with Figure 8. Paths are denoted by the edges. Transition states were found for every edge of the cube and nowhere else. The energy rank of transition states is indicated by italic text adjacent to an edge. Edge arrows point from higher to lower energy on the  $t = 1.69$  surface. Note that minimum 4 from the undeformed surface is the global minimum on the deformed surface.

## Potential Smoothing and Simulated Annealing for Global Optimization

In the following section we quantify the efficiency of potential smoothing and simulated annealing as global optimization tools for CDAP. The global minimum for CDAP has an energy of  $-352.2535$  kJ/mol and the second lowest minimum has an energy of  $-351.1075$  kJ/mol (see Table II).

### POTENTIAL SMOOTHING

We used the diffusion equation method (DEM) of Scheraga and coworkers<sup>20</sup> for global optimization based on potential smoothing. The algorithm proceeds as follows:

- The original potential function  $E(\mathbf{r})$  is replaced by a transformed function  $U(\mathbf{r}, t)$  [see eq. (1)], where  $t$  is the deformation parameter. The parameter  $t$  is initially set to a large value at which level minimizations from random starting conformations converge to a unique minimum on the deformed convex PES.
- The smoothing parameter is slowly reduced according to a chosen reversal schedule followed by minimizations on each level until  $t = 0$  at which point the original PES is reached.

A crossing between minimum 4 and the global minimum occurs for  $t = 0.1372$ , i.e.,  $E(4) < E(1)$  for all values of  $t \geq 0.1372$ . For the DEM reversal schedule, we choose the deformation  $t_i$  according to

$$t_i = t_{\max} \left( \frac{n-i}{n} \right)^q$$

with  $t_{\max} = 60$ ,  $n = 100$ , and  $q = 3$ . The level of smoothing is adiabatically lowered from  $t_{\max}$ , followed by minimization. A quadratic or quartic schedule yields identical results for the DEM calculation. This reversal procedure converges to minimum 4 on the PES for  $t = 0$ . The mergers of minima 1, 2, and 3 with minimum 4 are preceded by crossings, i.e., there is a level of smoothing for which  $E(i) > E(4)$ ,  $i = \{1, 2, 3\}$  prior to their mergers. These crossings preclude the possibility that a procedure like DEM will converge to the global minimum.

### SIMULATED ANNEALING

We use two approaches to study relaxation to the global minimum based on simulated annealing. The fully enumerated PES for CDAP can be

used to compute time-dependent occupation probabilities for each minimum at different temperatures using a master equation formalism<sup>49–51</sup> derived from the equilibrium transition-state theory.<sup>52</sup> In the transition-state theory the rate constant for transitions between a pair of minima is approximated as the flux through the saddle region separating the two states. Because this flux is an equilibrium property, one need not perform actual dynamics to quantify transitions between individual states. Rather, the energies and local curvature at the minima and saddle points are sufficient to compute a rate constant. This is valid only in the limit of time scales considerably longer than the vibrational relaxation rates.<sup>10, 13, 49, 50, 52</sup>

For CDAP, there are 142 minima connected through 1038 transition states. Not all minima are directly connected, and there are redundant paths between various pairs of minima. If two minima are connected via more than one path, we choose the path corresponding to the smallest energy barrier. This sort of pruning results in 688 paths between unique pairs of minima. Using transition state theory and a set of initial conditions, we can estimate the likelihood of populating a state  $i$  as a function of time  $\tau$  at a prescribed temperature  $T$ . This is done by calculating the  $N \times N$  rate matrix  $\mathbf{R}$  whose elements  $R_{ij}$  denote probabilities for a transition from state  $j$  to state  $i$ . The time evolution of the  $N$ -component vector  $P(\tau)$  may be written as:

$$\frac{dP}{d\tau} = \mathbf{R}P(\tau) \quad (9)$$

where

$$\frac{dP_i}{d\tau} = \sum_j [R_{ij}P_j(\tau) - R_{ji}P_i(\tau)]$$

The elements  $R_{ij}$  of the rate matrix, in units of (s)<sup>-1</sup>, are greater than or equal to zero, and the sum over each column of the matrix is exactly equal to unity to ensure conservation of probability. The rate constant for a transition from state  $j$  to state  $i$  is calculated in terms of the energy barrier  $E_b^{ij}$ , the temperature parameter  $RT$ , where  $R$  is the ideal gas constant in units of kJ/mol/K, and the density of states  $Z_{ij}^\ddagger$  and  $Z_j$  for the transition state and minimum  $j$ , respectively.  $R_{ij}$  is given by the Arrhenius rate formula of the form:

$$R_{ij} = \left[ \frac{RT}{h} \right] \frac{Z_{ij}^\ddagger}{Z_j} \exp\left(-\frac{E_b^{ij}}{RT}\right) \quad (10)$$

The weights  $Z_{ij}^\ddagger$  and  $Z_j$  are calculated in the harmonic approximation as the product of  $n_v - 1$

positive vibrational modes at the saddle point and  $n_v$  vibrational nodes at the minimum, respectively, where  $n_v$  is the number of vibrational degrees of freedom.<sup>52</sup>

The solution to eq. (9) can be written as:

$$P(\tau) = P_{\text{eq}} + \sum_{i (\lambda_i < 0)} C_i \Lambda_i \exp\{\lambda_i \tau\} \quad (11)$$

where  $\lambda_i$  denote nonzero eigenvalues of the rate matrix  $\mathbf{R}$ ,  $\Lambda_i$  is the  $i$ th eigenvector,  $P_{\text{eq}}$  is the  $N$ -component vector of equilibrium occupation probabilities at temperature  $T$  and  $C_i$  is a normalization factor determined using the initial conditions  $P$  at  $\tau = 0$ . Eigenvalues of  $\mathbf{R}$  are characteristic relaxation rates for the different eigenstates of the system at temperature  $T$ . All eigenvalues  $\lambda_i$  of the rate matrix  $\mathbf{R}$  have to be less than or equal to zero and the zero eigenvalue corresponds to the stationary state.

The length of the simulation required to isolate the global minimum in simulated annealing grows exponentially with size of energy scales on the PES. Though eq. (11) suggests exponential relaxation to the equilibrium distribution, values of  $\lambda_i \approx 0$  will result in very slow convergence to equilibrium. The largest nonzero eigenvalue sets the upper limit on the rate of convergence to equilibrium. If the success of simulated annealing is based on realizing the equilibrium distribution at each temperature, we should be able to estimate the simulation length needed to converge to the global minimum.

The occupation probabilities at time  $\tau$  for a given temperature  $T$  and initial conditions  $P(0)$  are given by the vector  $P(\tau)$ . If  $\varepsilon$  is an infinitesimally small positive number, then convergence to equilibrium can be measured in terms of the largest nonzero eigenvalue  $\lambda_{\text{max}}$  using:  $|P(\tau) - P_{\text{eq}}| = \varepsilon \approx C_{\text{max}} \Lambda_{\text{max}} \exp|\lambda_{\text{max}} \tau_{\text{eq}}| \sim \exp|\lambda_{\text{max}} \tau_{\text{eq}}|$  or  $\tau_{\text{eq}} \propto 1/|\lambda_{\text{max}}|$ . Here,  $\tau_{\text{eq}}$  is the time to equilibration and  $|\lambda_{\text{max}}|$  is the magnitude of the largest eigenvalue of the rate matrix  $\mathbf{R}$ . Because all nonzero eigenvalues  $\lambda_i$  are negative,  $|\lambda_{\text{max}}| \approx 0$  would imply very slow convergence to equilibrium.

For CDAP, we computed the largest nonzero eigenvalue of the rate matrix to obtain an estimate for  $\tau_{\text{eq}}$  at different temperatures,  $T$ . Clearly,  $|\lambda_{\text{max}}|$  will deviate from zero as temperature increases. Table V shows the values of  $\lambda_{\text{max}}$  obtained by diagonalizing the rate matrix at different values of  $T$ . The parameter  $\tau_{\text{eq}}$  is estimated as  $1/|\lambda_{\text{max}}|$ . From the data in Table V it is clear that a simulation on the order of at least 1 s will be required to optimize the likelihood of convergence to the global minimum.

**TABLE V.**  
**Variation of  $\lambda_{\max}$  for CDAP as a Function of Temperature.**

Temperature (Kelvin)	$\lambda_{\max}$ (s) <sup>-1</sup>	$\tau_{\text{eq}} \sim \{1/ \lambda_{\max} \}$ (s)
100	$-7.53 \times 10^{-27}$	$1.32 \times 10^{26}$
125	$-1.56 \times 10^{-19}$	$6.40 \times 10^{18}$
150	$-3.96 \times 10^{-14}$	$2.55 \times 10^{13}$
175	$-2.83 \times 10^{-10}$	$3.53 \times 10^9$
200	$-2.22 \times 10^{-7}$	$4.50 \times 10^6$
225	$-3.93 \times 10^{-5}$	$2.54 \times 10^4$
250	$-2.45 \times 10^{-3}$	408.30
275	$-7.15 \times 10^{-2}$	13.98
300	-1.19	0.85
325	-12.78	$7.82 \times 10^{-2}$
350	-98.36	$1.01 \times 10^{-2}$
375	-579.09	$1.73 \times 10^{-3}$
400	$-2.74 \times 10^3$	$3.64 \times 10^{-4}$
425	$-1.09 \times 10^4$	$9.17 \times 10^{-5}$
450	$-3.73 \times 10^4$	$2.68 \times 10^{-5}$
475	$-1.13 \times 10^5$	$8.88 \times 10^{-6}$
500	$-3.06 \times 10^5$	$3.27 \times 10^{-6}$
525	$-7.56 \times 10^5$	$1.32 \times 10^{-6}$
550	$-1.73 \times 10^6$	$5.79 \times 10^{-7}$
575	$-3.67 \times 10^6$	$2.72 \times 10^{-7}$
600	$-7.36 \times 10^6$	$1.36 \times 10^{-7}$

### MASTER EQUATION CALCULATIONS TO SIMULATE SIMULATED ANNEALING

The protocol used is as follows: we set up a cooling schedule between  $T_{\text{high}} = 600$  K and  $T_{\text{low}} = 100$  K. The value for  $T_{\text{high}}$  is an overestimate for the validity of the master equation formalism; therefore, the results must be interpreted with caution. Results are valid inasmuch as it probes the slowest step in simulated annealing for CDAP, i.e., relaxation to the global minimum hindered by a large energy barrier between the ground state and the rest of the PES. The simulation is started by setting the temperature to 600 K,  $P(142) = 1$  and  $P(i) = 0$  for all  $i \neq 142$ ;  $P_i(\tau)$  is computed for each of the states by setting a value for  $\tau$  and using the solution given in eq. (11).  $\tau$  is set to a value of at least 1 ns because the master equation formalism is not valid for smaller time intervals. The distribution of probabilities  $P_i(\tau)$  ( $i = 1, \dots, 142$ ) for  $T = T_{\text{high}}$  is used as the initial condition for  $T = T_{\text{high}} - \Delta T$ , the next temperature value along the cooling schedule. This procedure is iterated until  $T = T_{\text{low}}$  is reached.

The two parameters that determine the results of a master equation simulation are the cooling sched-

ule and the value chosen for  $\tau$  at each temperature level  $T$ . Results of our calculations are sensitive to values chosen for  $\tau$  and are relatively insensitive to details of the cooling schedule. We use a linear cooling schedule that decreases the temperature from 600 to 100 K in intervals of 25 K for a total of 21 steps in the protocol. Figure 10 shows the evolution of occupation probabilities for the global minimum and the second lowest minimum as a function of temperature obtained from master equation simulations for different values of  $\tau$  ranging from 1 ns to  $10^4$  s. For small values of  $\tau$ , higher lying states other than minimum 1 and minimum 2 have significant occupation probabilities at the end of the simulation. As  $\tau$  is increased, the occupation probabilities are divided between the ground state and second lowest energy state, with longer values of  $\tau$  being necessary to increase the likelihood of populating the global minimum.

The results shown in Figure 10 can be explained in terms of the distribution of energy barriers on the PES and the equilibrium occupation probabilities for the different states as a function of temperature. For temperatures lower than 400 K, barriers connecting minimum 1 to the rest of the PES are not easily overcome, resulting in an increased flux into minimum 2. This leads to longer values of  $\tau$  to obtain higher occupation probabilities for the ground state relative to other states on the PES. The master equation simulations set an upper limit on the length of simulation required for a simulated annealing protocol to converge to the global minimum. Enhanced sampling at higher temperatures does not facilitate convergence to the global minimum because the ensemble at high temperature does not favor the global minimum. Results for different values of  $\tau$ , Figure 10, are consistent with the estimates in Table V, which suggests that a simulation of at least 1 s may be required. This is set by the magnitude of  $\lambda_{\max}$  for  $T = 300$  K, the temperature at which the equilibrium probability for populating the global minimum is greater than 0.5.

### MOLECULAR DYNAMICS SIMULATED ANNEALING (MDSA) FOR CDAP

Multiple molecular dynamics simulated annealing (MDSA) runs for CDAP were performed to study the likelihood of convergence to the global minimum. Our expectation from the master equation calculations would be that in a hundred independent MDSA runs, for trajectories in the vicinity of a nanosecond, the global minimum will be found less than 10% of the time, whereas the second lowest

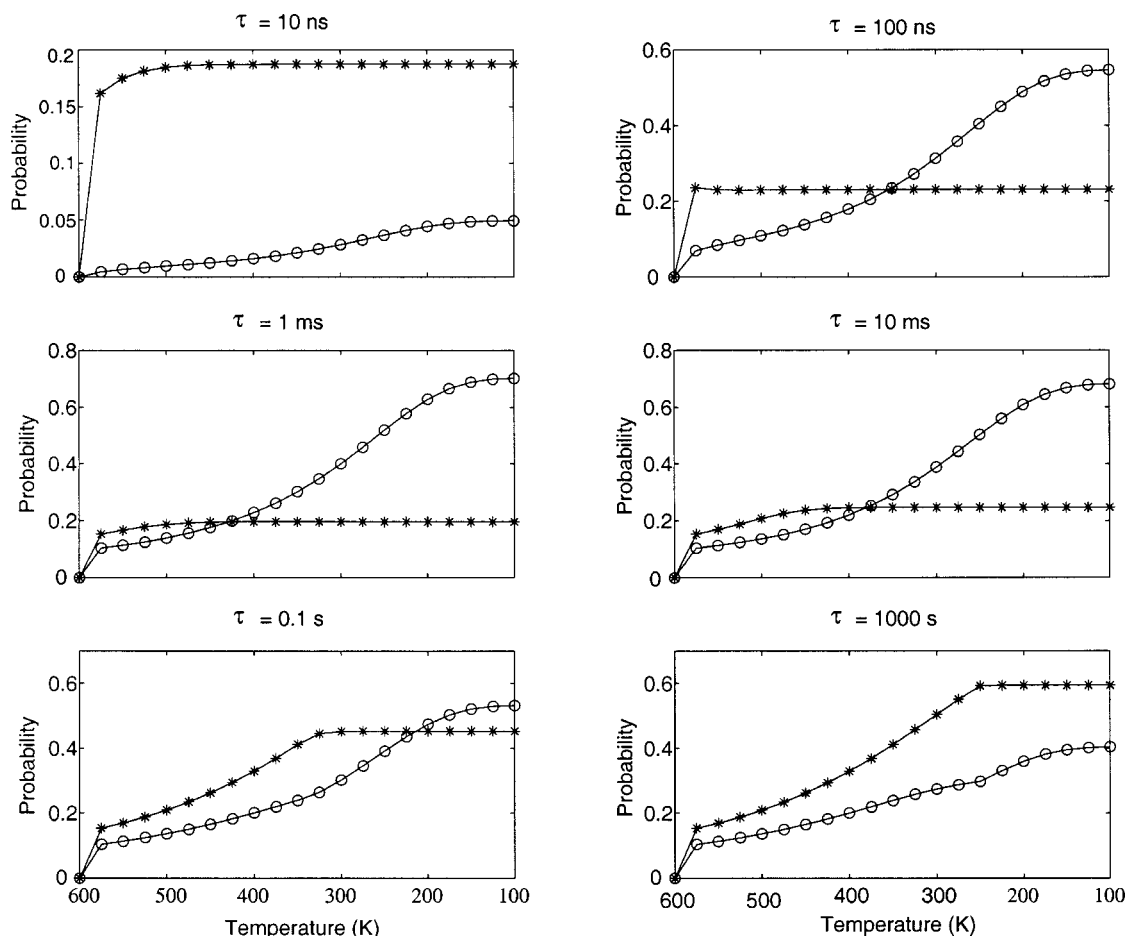


**FIGURE 10.** Master equation trajectories for  $P_1(\tau)$  and  $P_2(\tau)$ , the occupation probabilities of the global minimum ( $-*$ ) and the second lowest minimum ( $-o-$ ) are shown as a function of temperature for different values of total  $\tau$ . The value for  $\tau$  shown in each of panel corresponds to the actual value used in eq. (11) to compute  $P_i(\tau)$  at each of 21 temperature levels every 25 K between 600 and 100 K. Thus, the total time represented by each panel is  $21\tau$ . Each simulation is started by setting  $P_{142}(0) = 1$ , i.e., the occupation probability for the highest lying minimum is initially 1 at  $T = 600$  K. The initial step comprises of a rapid flux out of the highest lying minimum into low lying regions. This is shown quite clearly in the  $\tau = 10$  ns simulation, where the first time segment is characterized by a relaxation into low-lying regions on the PES. For simulations with total simulation time  $\tau$  ranging from 10 ns to 1  $\mu$ s, the final occupation probability for the global minimum asymptotes to a value of 0.2. This value is the equilibrium occupation probability for the global minimum at high temperatures. As temperature is lowered, energy barriers separating the global minimum from the rest of the PES become more pronounced, and there is no flux into the ground state. The second-lowest energy minimum is connected via numerous low energy barriers to other minima on the PES. For simulations longer than  $\tau = 10$  ns local equilibrium is achieved within the catchment region of minimum 2 and there is an increased likelihood of a simulated annealing protocol converging to the second lowest minimum on the PES. If simulated annealing is to consistently succeed in finding the global minimum, then the probability of finding the global minimum at the end of a master equation simulation has to be better than 0.5. The master equation simulations suggest that a simulation trajectory of length greater than a few milliseconds would be required in order for  $P_1(\tau)$  to approach 0.5. The results shown in this figure are in accord with estimates for the slowest events as a function of temperature summarized in Table V.

minimum will be found better than 50% of the time. The initial conformation for all MDSA runs is minimum 142. We generated 100 independent 0.5-ns trajectories of MDSA using the following parameters for each trajectory: a 1.0-fs time step,  $5 \times 10^5$

steps of MD, and a sigmoidal cooling schedule between 5000 and 0 K.

Starting from minimum 142, 8 of the 100 trajectories converge to the global minimum. Forty-seven of the trajectories converge to minimum 2, 6 to min-



imum 4, and 15 to minimum 8. Comparing these results to the master equation simulations suggests a discrepancy close to three orders of magnitude in favor of the MDSA runs. There are two reasons for this discrepancy: (1) The MDSA runs do not perform equilibration steps at each temperature level along the cooling schedule, and (2) some of the more general assumptions of classical transition state theory could build in errors into the estimates from the master equation simulations. These assumptions include zero recrossing in saddle regions, dependence of the rate constant only on the flux at the dividing surface, and use of the harmonic approximation to estimate entropies. The results of the MDSA runs indicate that estimates from Table V and Figure 10 should be relaxed by a couple of orders of magnitude. The smallest barrier for a transition from minimum 2 to minimum 1 is 81.6 kJ/mol. At high enough temperatures where this transition is rapid, the system is in fast equilibrium between all accessible minima. Barriers between higher lying minima and minimum 2 are considerably smaller than 81.6 kJ/mol. The thermodynamic ensemble changes at temperatures higher than 300 K vis-à-vis the relative occupation probabilities of minimum 1 and all other states. Therefore, for temperatures where the global minimum becomes favored, the barrier between minimum 1 and the rest of the PES is too high to negotiate via thermal activation.

### Shifting in Potential Smoothing and Simulated Annealing

If the multidimensional potential function  $E(\mathbf{r})$  were perfectly isotropic, spatial averaging as shown in eq. (1) would yield a smoothed function  $U(\mathbf{r}, t)$  for which the location of the minimum  $\mathbf{r}_0$  remains unchanged. However, most molecular mechanics functions are inherently anisotropic, leading to a shifting of  $\mathbf{r}_0$  as a function of  $t$ . For instance, if  $E(\mathbf{r})$  represents a three-dimensional DOPLS Gaussian van der Waals interaction potential written as  $E(\mathbf{r}) = a_1 \exp\{-b_1 r^2\} + a_2 \exp\{-b_2 r^2\}$ , then the location of the minimum  $\mathbf{r}_0$  can be written as

$$\mathbf{r}_0 = \ln \left\{ \frac{-b_1 a_1}{b_2 a_2} \right\}$$

For nonzero values of  $t$ ,

$$a_i \rightarrow \frac{a_i}{\{1 + 4b_i t\}^{3/2}} \quad \text{and} \quad b_i \rightarrow \frac{b_i}{\{1 + 4b_i t\}}$$

and

$$\mathbf{r}_0 = \ln \left\{ \frac{-b_1 a_1}{b_2 a_2} \right\}$$

**TABLE VI.**  
Shifting of Minima as a Function of Deformation  $t$ .

$t$	Angular Deviations (deg)			
	$\phi_1$	$\psi_1$	$\phi_2$	$\psi_2$
0.00000	-83.89	67.73	-82.79	65.80
0.00005	-83.91	67.74	-82.80	65.81
0.00040	-83.98	67.82	-82.88	65.89
0.00135	-84.19	68.04	-83.11	66.10
0.00320	-84.61	68.47	-83.55	66.52
0.00625	-85.30	69.20	-84.27	67.21
0.01080	-86.31	70.32	-85.33	68.28
0.01715	-87.72	72.00	-86.79	69.84
0.02560	-89.57	74.37	-88.67	72.06
0.03645	-91.93	77.84	-91.00	75.25
0.05000	-94.91	83.18	-93.79	79.96

The extent of shifting is measured by the deviations of  $\langle \phi_1, \psi_1 \rangle$  and  $\langle \phi_2, \psi_2 \rangle$  for minimum 2 of CDAP from their  $t = 0$  values. For  $t = 0$ ,  $\langle \phi_{1(0)}, \psi_{1(0)} \rangle = \langle -83.89^\circ, 67.73^\circ \rangle$  and  $\langle \phi_{2(0)}, \psi_{2(0)} \rangle = \langle -82.79^\circ, 65.8^\circ \rangle$ . The deviations increase as the PES becomes smoother, and is a measure of the anisotropy of the undeformed surface.

leads to a change in the value of  $\mathbf{r}_0$  upon increase in the value of  $t$ , i.e., the location of the minimum shifts as a function of increased deformation.

We use minimum 2 as a representative for a comparison of shifting in potential smoothing and temperature-controlled molecular dynamics. Table VI shows values for shifting in terms of the torsional angles  $\langle \phi_1, \psi_1 \rangle$  and  $\langle \phi_2, \psi_2 \rangle$  for minimum 2. The original values for these angles are  $\langle \phi_{1(0)}, \psi_{1(0)} \rangle = \langle -83.89^\circ, 67.73^\circ \rangle$  and  $\langle \phi_{2(0)}, \psi_{2(0)} \rangle = \langle -82.79^\circ, 65.8^\circ \rangle$ . Only small values of  $t$  are shown because the shifting is influenced by the basin that minimum 2 merges into for larger values of  $t$ .

For minimum 2 of CDAP, the time averaged values of  $\langle \phi_1, \psi_1 \rangle$  and  $\langle \phi_2, \psi_2 \rangle$  change as a function of temperature in keeping with the anisotropy of the PES. We generated 11.5-ns dynamics trajectories for different values of the system temperature  $T$ . The first 500 ps were set aside as equilibration steps. Coordinate snapshots were generated at every picosecond of simulation, and used to compute the average values of the backbone dihedral angle pairs,  $\langle \phi_1, \psi_1 \rangle$  and  $\langle \phi_2, \psi_2 \rangle$ , over the trajectory. Shifting is measured by the deviation of  $\langle \phi_1, \psi_1 \rangle$  and  $\langle \phi_2, \psi_2 \rangle$  from  $\langle \phi_{1(0)}, \psi_{1(0)} \rangle$  and  $\langle \phi_{2(0)}, \psi_{2(0)} \rangle$ , where the latter are the  $T = 0$  K values. Only trajectories for lower values of  $T$  are used because these trajectories are confined to the basin of minimum 2, and can be correctly interpreted as shifting of the local minimum not influenced by nonlocal basins on the PES. Re-

**TABLE VII.**  
**Shifting of Minima as a Function of Temperature  $T$ .**

$T$	Angular Deviations (deg)			
	$\phi_1$	$\psi_1$	$\phi_2$	$\psi_2$
50	-84.42	68.32	-83.46	66.43
75	-84.82	68.66	-83.58	66.68
100	-84.93	68.99	-84.00	66.98
125	-85.05	69.37	-84.53	67.16
150	-85.56	69.83	-84.89	67.61
175	-85.82	70.07	-85.23	68.00
200	-86.80	71.40	-86.03	68.15
225	-88.32	72.34	-87.06	68.92
250	-88.94	72.84	-88.72	69.12

The extent of shifting is estimated from the deviation of  $(\langle\phi_1\rangle, \langle\psi_1\rangle)$  and  $(\langle\phi_2\rangle, \langle\psi_2\rangle)$  from values at the corresponding energy minimum. Time-averaged values of torsional angles shown are for minimum 2 of CDAP generated from 11.5 ns molecular dynamics simulations at different temperatures. The energy minimum is at  $(\phi_{1(0)}, \psi_{1(0)}) = (-83.89^\circ, 67.73^\circ)$  and  $(\phi_{2(0)}, \psi_{2(0)}) = (-82.79^\circ, 65.8^\circ)$ . The deviations increase as temperature increases. Shifting is in the direction of the smallest energy barrier that connects minimum 2 and minimum 5 on the PES network for CDAP.

sults for the time-averaged values of  $\langle\phi_1, \psi_1\rangle$  and  $\langle\phi_2, \psi_2\rangle$  of minimum 2 computed from trajectories at different temperatures are summarized in Table VII. The data in Tables VI and VII show correlations between shifting of minimum 2 measured as a function of smoothing and temperature. The data in Tables VI and VII can be used to correlate values for  $t$  and  $T$  for shifting of each of the four torsional angles. These derived relations are shown in Figure 11.

## Crossings in Potential Smoothing and Simulated Annealing

Consider a system characterized by  $n$ -minima coupled to a heat bath at some temperature  $T$ . The equilibrium partition function for the  $n$ -minima of the canonical ensemble is written in terms of the Helmholtz free energy  $F_m = E_m - TS_m$  as

$$Z_{\min} = \sum_{m=1}^n \exp(-\beta F_m) \quad (12)$$

where  $\beta = (RT)^{-1}$ ;  $E_m$  and  $S_m$  are the potential energy and configurational entropy of minimum  $m$  at temperature  $T$ . The canonical partition function can

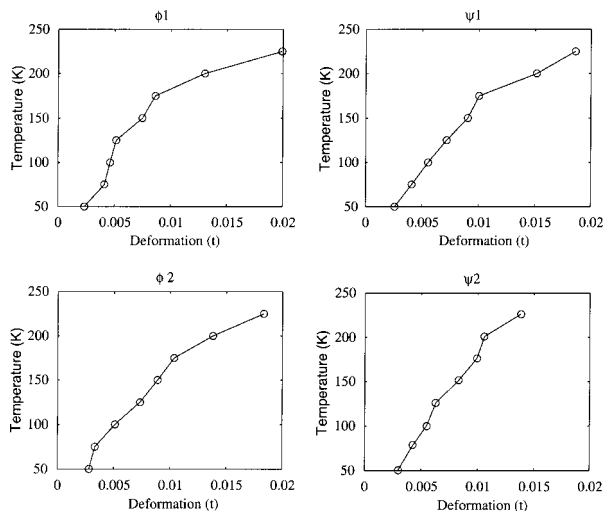


**FIGURE 11.** Derived curves for the shifting of  $\langle\phi_1, \psi_1\rangle$ ,  $\langle\phi_2, \psi_2\rangle$  of minimum 2 as a function of deformation and temperature based on the raw data from Tables VIII and IX. The points in each panel were generated by the interpolating level of deformation needed to give the amount of shifting observed at each 25 K temperature increment from 50 to 225 K.

be rewritten in the harmonic approximation as<sup>52</sup>

$$Z_{\min} = \sum_{m=1}^n \frac{\exp(-\beta E_m)}{(\beta h)^{n_v} \prod_{j=1}^{n_v} \Lambda_{m,j}} \quad (13)$$

where  $n_v$  is the number of vibrational degrees of freedom,  $h$  is Planck's constant, and  $\Lambda_{m,j}$  is the vibrational frequency of the  $j$ th normal mode at minimum  $m$ . Configurational entropy in the harmonic approximation is related to the product of the vibrational normal mode frequencies  $\Lambda_{m,j}$  at minimum  $m$ . The equilibrium occupation probability for minimum  $m$  is written in terms of the canonical partition function  $Z_{\min}$  as

$$P_m^{\text{eq}} = \frac{1}{Z_{\min}} \left( \frac{\exp(-\beta E_m)}{(\beta h)^{n_v} \prod_{j=1}^{n_v} \Lambda_{m,j}} \right) \quad (14)$$

Equilibrium probabilities for the 10 lowest minima of CDAP as a function of temperature are shown in Figure 12. For very low temperatures the global minimum has an equilibrium probability greater than 0.9. The figure shows that as temperature increases, equilibrium probability of the global minimum decreases while the equilibrium probabilities of higher lying minima increase, and that the relative free energies of pairs of minima also change. Crossings occur because the temperature-dependent entropic term in the denominator of eq. (14) influences each minimum independently.

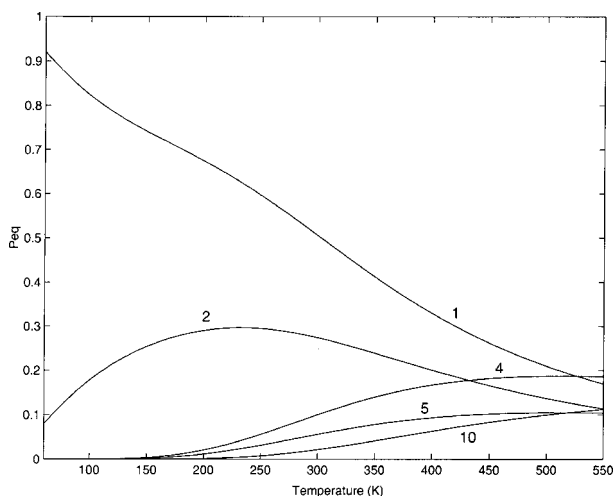


**FIGURE 12.** Equilibrium probabilities at various temperatures of the 10 lowest energy minima on the undeformed surface. Broad basins become entropically favored as temperature increases. In particular, as temperature increases, the narrow global minimum 1 becomes less favored and the broader basin 4, which is the “projected” basin on deformed surfaces, becomes the dominant state.

Figure 12 shows reordering of equilibrium probabilities as a function of temperature. For a pair of minima  $m_i$  and  $m_j$ ,  $P_{eq}(m_i)$  may be less than  $P_{eq}(m_j)$  at some temperature  $T = T_1$ . For a temperature  $T = T_2 > T_1$  there can be a reordering of minima, i.e.,  $P_{eq}(m_j)$  is now less than  $P_{eq}(m_i)$ , indicating a crossing in relative free energies for pairs of minima. This reflects a different ensemble due to the increase in temperature. We correlate temperature and smoothing values by comparing crossings of a pair of minima  $m_i$  and  $m_j$  in terms of  $t$  and  $T$ .

Consider two minima  $m_i$  and  $m_j$  that cross at some smoothing level  $t_1$  and two other unique minima  $m_k$  and  $m_l$  which cross at some smoothing level  $t_2 > t_1$ . If the relative occupation probabilities  $P_{eq}(m_i)$  and  $P_{eq}(m_j)$  cross at  $T = T_1$  and similarly  $P_{eq}(m_k)$  and  $P_{eq}(m_l)$  cross at  $T = T_2$ , a correlation between smoothing and temperature controlled crossings exist if  $T_2 > T_1$ . Table VIII lists all the crossings identified in terms of the relative energy values for a pair of minima of CDAP as a function of deformation and the relative equilibrium probabilities of the same pair as a function of the canonical ensemble temperature. We plot the correlation of  $t$  and temperature  $T$  using the data from Table VIII. This plot and a linear fit to the data are shown in Figure 13. At higher temperatures the harmonic approximation is inaccurate, and similarly, for higher values of smoothing a reduction in the number of

**TABLE VIII.**  
Comparison of Some of the Crossings between Pairs of Minima as a Function of Deformation  $t$  and Canonical Temperature  $T$  for CDAP.

Crossing	$t$	$T$ (K)
4 ⊗ 3	0.00125	6.0
5 ⊗ 3	0.00125	6.0
9 ⊗ 8	0.00288	26.0
10 ⊗ 8	0.0035	42.0
10 ⊗ 9	0.0048	59.0
12 ⊗ 8	0.0086	88.0
10 ⊗ 7	0.0097	67.0
9 ⊗ 7	0.0124	76.0
13 ⊗ 8	0.0130	125.0
10 ⊗ 3	0.0137	175.0
9 ⊗ 6	0.0144	215.0
12 ⊗ 6	0.0159	196.0
9 ⊗ 3	0.0184	259.0
12 ⊗ 3	0.0190	223.0
13 ⊗ 6	0.0202	230.0
13 ⊗ 3	0.0243	257.0
13 ⊗ 9	0.0439	253.0
7 ⊗ 3	0.02304	583.0
4 ⊗ 2	0.05895	432.0
4 ⊗ 1	0.15875	527.0

minima occurs due a series of mergings and the crossings across largely varying spatial scales. Figure 13 shows only the low  $T$  and low  $t$  region, i.e.,  $T < 300$  K and  $t < 1.6$ . The linear correlation coefficient for the plot of  $t$  and  $T$  in Figure 13 is  $r^2 = 0.95$ .

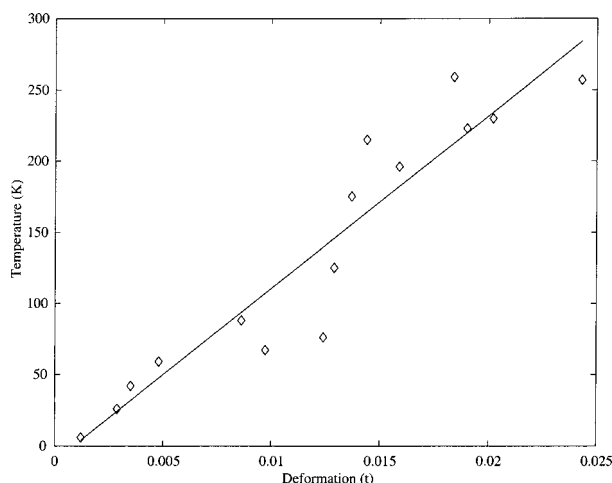


**FIGURE 13.** Correlation of crossing temperature ( $T$ ) and time ( $t$ ). The line is a least-squares fit to the data and has a correlation coefficient  $r^2 = 0.95$ .

## Discussion

### POTENTIAL SMOOTHING AND SIMULATED ANNEALING

We have studied the similarities between two methods, potential smoothing and simulated annealing, that exploit distinct features of potential energy surfaces. Results of our work are summarized below.

Both potential smoothing and simulated annealing sample conformational space in a hierarchical manner. The hierarchy in annealing is derived from the diverse energy scales, while the hierarchy in smoothing is derived from spatial scales on the PES. Neither measure is ad hoc, and both pertain to specific features of the topography of energy landscapes. In light of recent work<sup>2, 4, 8–10, 13, 15, 16</sup> it seems reasonable to expect some degree of correlation between the spatial and energy scales for potential energy surfaces of proteins and peptides.

Spatial scaling in potential smoothing derives from an analytical transformation of the potential function, see eq. (1). The topography of a smoothed PES is directly determined by prominent spatial features on the undeformed surface. In simulated annealing the underlying potential function is unchanged, but sampling weights derived from the Boltzmann machinery increase the likelihood of visiting higher energy regions as temperature increases.

The fine structure associated with numerous local minima can be averaged over to generate a many-to-few mapping in terms of a specific hierarchical control parameter. For small values of the appropriate parameter the number of basins equals the number of minima; for large values, all minima map into a single basin. In simulated annealing the mapping leads to a small number of temperature-dependent basins, and the partitioning is determined by larger energy barriers. In the case of CDAP these barriers are associated with *cis-trans* rotations. The basins obtained as a function of increased PES deformation probe the spatial separations between pairs of minima and their connecting transition states.<sup>38</sup> At the level of obtaining exactly eight basins in terms of  $T$  and  $t$  the two basin maps are very similar. Similarity is quantified in terms of the mutual overlap between each of the basins obtained (see Table IV and Figs. 5 and 8).

Equilibrium probabilities of minimum energy regions change with increasing temperature. In some cases, the ratio of weights for pairs of minimum energy regions get reversed. An analogous phe-

nomenon occurs on smooth energy surfaces in which case the crossing between pairs of minima is recorded in terms of the energy function values. Similar crossing patterns in terms of temperature and deformation are observed for CDAP, and are summarized in Table VIII.

An increase in temperature is accompanied by excursions of the system away from the location of a local minimum. Because conformational space at a finite temperature is sampled according to the Boltzmann weight at that temperature, the average value for the location of the minimum will deviate away from the  $T = 0$  K value. If the system does not leave the basin of attraction of a local minimum, then the average value computed from a sample trajectory pertains to the volume of the basin. In spatial averaging, the position of the local minimum shifts in keeping with the convolution of the original potential function. We find that positional shifting in the location of a stable local minimum of CDAP is quite similar in both cases, as can be seen in Tables VI and VII.

Given the analogies between simulated annealing and potential smoothing we expect the latter to be a more efficient method for conformational sampling because the search process is deterministically focused into specific catchment regions, whereas in simulated annealing this is done in a probabilistic way. It has been demonstrated that potential smoothing lends itself to simple search algorithms, such as a series of local minimizations combined with local searches,<sup>36</sup> which are efficient and scale reasonably with the size of the system. Simulated annealing is inefficient because it requires either a Markov chain trajectory in Metropolis Monte Carlo sampling or a time series trajectory in MDSA, and the extent of searching in trajectory methods scales exponentially as the size of the system.

### COMPARISON OF THE CONFORMATIONAL NETWORKS OF CDAP AND ISOBTURYL-(ALA)<sub>3</sub>-NH-METHYL

Czerminski and Elber have described<sup>13</sup> a network of 138 minima and 490 transition states of isobuturyl-(ala)<sub>3</sub>-NH-methyl (IAN) on the CHARMM PES. LAN consists of 26 united atom centers; CDAP consists of 18. We find more minima and transition states in CDAP than in IAN. This difference is probably due to the diversity of initial conformations used to locate minima and transition states for CDAP, and the differences between the DOPLS and CHARMM potential energy surfaces. In both systems, reaction path predictions lead to

transition states, and minimization from these states are used to connect the pair of minima on a path. The reaction path method has a strong tendency to traverse the volume of conformational space bounded by initial structures used to compute reaction paths, but may not be useful by itself as a tool for exploring conformational space.

Czermanski and Elber<sup>13,46</sup> found 502 transition states out of  $139 \times 138/2 = 9591$  possible pairwise paths (5.2%). In contrast, the present search found 1038 transitions from a possible 10,011 paths (10.5%). These 1038 states include "degenerate rearrangements" and redundant paths. The 1038 transition states represent only 688 unique connections between minima, i.e., many transition states represent redundant paths between the same pairs of minima. On average, each IAN minimum is connected to  $2 \times 393/139 \approx 5.6$  others, whereas the minima for CDAP are connected to  $2 \times 688/142 \approx 9.7$  others. This implies that peptide conformations are quite extensively interconnected.

The main distinction between our work and that of Czermanski and Elber is our observation that paths exist between distant regions of conformational space. They note that most transitions involve 1 or 2 dihedral angle changes, but we find that 18% of the paths connect structures that differ in three conformational descriptors. This observation suggests that conformational transitions may involve concerted movements of several degrees of freedom, and connect very distant regions of conformational space.

Our results suggest that potential energy surfaces may have fairly pronounced features. Specifically the redundancy of transition states connecting lower energy regions of the PES suggests the possibility of multiple routes into low energy regions. This is part of the hypothesis of landscape models for protein folding.<sup>8,9</sup>

## Acknowledgments

All computer programs used for calculations reported in this work are part of the TINKER molecular modeling package, and are available from the authors. R.V.P. thanks Dr. Kamal Bhattacharya for helpful discussions, and Prof. Garland R. Marshall for support.

## References

- Brooks, C. L., III; Karplus, M.; Pettitt, B. M. *Proteins: A Theoretical Perspective of Dynamics, Structure, and Thermodynamics*; John Wiley and Sons: New York, 1988.
- Church, B. W.; Ulitsky, A.; Shalloway, D. *Adv Chem Phys* 1999, 105, 273.
- Straub, J. E.; Rashkin, A. B.; Thirumalai, D. *J Am Chem Soc* 1994, 116, 2049.
- Sherrington, D. *Physica D* 1997, 107, 117.
- Rammal, R.; Toulouse, G.; Virasoro, M. A. *Rev Mod Phys* 1986, 58, 765.
- Thirumalai, D.; Mountain, R. D.; Kirkpatrick, T. R. *Phys Rev A* 1989, 39, 3563.
- Wales, D. J.; Miller, M. A.; Walsh, T. R. *Nature* 1998, 394, 758.
- Onuchic, J. N.; Luthey-Schulten, Z.; Wolynes, P. G. *Annu Rev Phys Chem* 1997, 48, 545.
- Dill, K. A.; Chan, H. S. *Nature Struct Biol* 1997, 4, 10.
- Becker, O. M.; Karplus, M. *J Chem Phys* 1997, 106, 1495.
- Honeycutt, J. D.; Thirumalai, D. *Proc Natl Acad Sci USA* 1990, 87, 3526.
- Straub, J. E.; Thirumalai, D. *Proc Natl Acad Sci USA* 1993, 90, 809.
- Czermanski, R.; Elber, R. *J Chem Phys* 1990, 92, 5580.
- Mézard, M.; Parisi, G. *J Chem Phys* 1999, 111, 1076.
- Fraunfelder, H.; Sligar, S. G.; Wolynes, P. G. *Science* 1991, 254, 1598.
- Straub, J. E.; Thirumalai, D. *Proteins* 1993, 15, 360.
- Nienhaus, G. U.; Müller, J. D.; McMahon, B. H.; Fraunfelder, H. *Physica D* 1997, 107, 297.
- Velikson, B.; Bascle, J.; Garel, T.; Orland, H. *Macromolecules* 1993, 26, 4791.
- Kirkpatrick, S.; Gelatt, C. D., Jr.; Vecchi, M. P. *Science* 1983, 220, 671.
- Piela, L.; Kostrowicki, J.; Scheraga, H. A. *J Phys Chem* 1989, 93, 3339.
- Ma, J.; Straub, J. E. *J Chem Phys* 1994, 101, 533.
- Barker, K.; Henderson, D. *Rev Mod Phys* 1976, 48, 587.
- Binder, K.; Heermann, D. W. *Monte Carlo Simulation in Statistical Physics: An Introduction*, Springer-Verlag: New York, 1998, 3rd ed.
- Brünger, A. T.; Kuriyan, J.; Karplus, M. *Science* 1987, 235, 458.
- Aarts, E.; Korst, J. *Simulated Annealing and Boltzmann Machines*; John Wiley and Sons: New York, 1989.
- Straub, J. E. In *Recent Developments in Theoretical Studies of Proteins*; Elber, R., Ed.; World Scientific: Singapore, 1996; p. 135.
- van Laarhoven, P. J. M.; Aarts, E. H. L. *Simulated Annealing: Theory and Applications*; D. Reidel: Dordrecht, 1987.
- Doye, J. P. K.; Wales, D. J. *Phys Rev Lett* 1998, 80, 1357.
- Doye, J. P. K.; Wales, D. J. *J Chem Phys* 1996, 105, 8428.
- Kostrowicki, J.; Piela, L.; Cherayil, B. J.; Scheraga, H. A. *J Phys Chem* 1991, 95, 4113.
- Shalloway, D. In *Recent Advances in Global Optimization*; Floudas, C. A.; Pardalos, P. M., Eds.; Princeton University Press: Princeton, NJ, 1992; p. 433.
- Moré, J. J.; Wu, Z. In *Large-Scale Optimization with Applications, Part III*; Biegler, L. T.; Coleman, T. F.; Conn, A. R.; Santosa, F. N., Eds.; Springer-Verlag: New York, 1996; p. 99.
- Amara, P.; Straub, J. E. *Phys Rev B* 1996, 53, 13857.
- Li, Z.; Scheraga, H. A. *Proc Natl Acad Sci USA* 1987, 84, 6611.
- Wales, D. J.; Doye, J. P. K. *J Phys Chem A* 1997, 101, 5111.

36. Pappu, R. V.; Hart, R. K.; Ponder, J. W. *J Phys Chem B* 1998, 102, 9725.
37. Tsao, C.; Brooks, C. L., III *J Chem Phys* 1994, 101, 6405.
38. Andricioaei, I.; Straub, J. E. *J Comput Chem* 1998, 19, 1445.
39. Ball, K. D.; Berry, R. S.; Kunz, R. E.; Li, F.-Y.; Proykova, A.; Wales, D. J. *Science* 1996, 271, 963.
40. Ponder, J. W. TINKER: Software Tools for Molecular Design, Version 3.7; available from <http://dasher.wustl.edu/tinker/>.
41. Jorgensen, W. L.; Tirado-Rives, J. *J Am Chem Soc* 1988, 110, 1657.
42. Brooks, B. R.; Brucoleri, R. E.; Olafson, B. D.; States, D. J.; Swaminathan, S.; Karplus, M. *J Comput Chem* 1983, 8, 187.
43. Amara, P.; Straub, J. E. *J Phys Chem* 1995, 99, 14840.
44. Ponder, J. W.; Richards, F. M. *J Comput Chem* 1987, 8, 1016.
45. Zimmerman, S. S.; Pottle, M. S.; Némethy, G.; Scheraga, H. A. *Macromolecules* 1977, 10, 1.
46. Czerminski, R.; Elber, R. *Proc Natl Acad Sci USA* 1989, 86, 6963.
47. Wales, D. J.; Walsh, T. R. *J Chem Phys* 1996, 105, 6957.
48. Shenkin, P. S.; McDonald, D. Q. *J Comput Chem* 1994, 15, 899.
49. Ball, K. D.; Berry, R. S. *J Chem Phys* 1998, 109, 8557.
50. Berry, R. S.; Breitengraser-Kunz, R. *Phys Rev Lett* 1995, 74, 3951.
51. Forst, W. *Theory of Unimolecular Reactions*; Academic Press: New York, 1973.
52. Hanggi, P.; Talkner, P. H.; Borkovec, M. *Rev Mod Phys* 1990, 62, 251.